

STRUCTURAL, ELECTRONIC AND MAGNETIC PROPERTIES OF DOPED WIDE BAND GAP SEMICONDUCTORS

**THESIS SUBMITTED FOR THE DEGREE OF
DOCTOR OF PHILOSOPHY (SCIENCE)
OF THE
JADAVPUR UNIVERSITY**

SEPTEMBER, 2009

MANOJ KUMAR YADAV

**SATYENDRANATH BOSE NATIONAL CENTRE
FOR BASIC SCIENCES
JD BLOCK, SECTOR 3, SALT LAKE CITY
KOLKATA 700 098, INDIA**

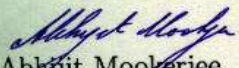
CERTIFICATE FROM THE SUPERVISOR

This is to certify that the thesis entitled "**Structural, electronic and magnetic properties of doped wide band gap semiconductors**" submitted by Manoj Kumar Yadav, who got his name registered on 2nd May, 2008 for the award of Ph.D. (Science) degree of Jadavpur University, is absolutely based upon his own work under the supervision of Professor Abhijit Mookerjee of S.N. Bose National Centre For Basic Sciences, Kolkata, India, and that neither this thesis nor any part of it has been submitted for either any degree/diploma or any other academic award anywhere before.

ABHIJIT MOOKERJEE

Sr. Professor & Dean (Faculty)

**S. N. Bose National Centre for Basic Sciences
Block - JD, Sector - III, Salt Lake - 700 098**


Abhijit Mookerjee

Senior Professor and Head, Materials Science Department,
Dean (Faculty),
Satyendranath Bose National Centre For Basic Sciences,
JD Block, Sector III, Salt Lake City, Kolkata 700 098
India

Date : 02.09.09

To my lovely niece,

Kittoo

Acknowledgments

The five years journey toward this thesis is about to come to an end. During these years I have been accompanied and supported by many people. It is the time now to express my gratitude to all of them who directly and indirectly contributed to make the journey easier.

First of all I would like to extend my sincere thank and gratitude to my thesis supervisor Prof. Abhijit Mookerjee. All these years he encouraged, inspired and guided me toward this goal. The kind of freedom he gave me in choosing research problems and making internal, external collaborations was crucial to my achieving this goal. I feel privileged to have had the opportunity to work under his excellent supervision.

I would like to thank Dr. Biplab Sanyal of Uppsala University who was my supervisor during my six months' stay in Sweden as a Guest Scholar. His inspiration lead me to carry out research in the field of diluted magnetic semiconductors. I am impressed by his friendly way of giving instructions. I would also like to thank Swedish Institute for granting me the Guest Scholarship.

I would like to thank Prof. A K Raychoudhuri, Director of S N Bose National Centre, for his valuable suggestions and for various facilities I enjoyed at the centre. I am also thankful to Prof. S. K. Sharma under whom I carried out my Post M. Sc. project work.

I would like to thank thesis committee members Prof. J K Bhattacharya, Dr. Indra Das Gupta, Dr. Tanusri Saha Das Gupta, and Dr. Priya Mahadevan for their valuable suggestions which I have incorporated in the thesis. I am also thankful to Dr. Ranjan Choudhary and Dr. Ranjit Bishwas for useful discussions and valuable suggestions.

I am thankful to Prof. Olle Eriksson for valuable discussions and for providing me various facilities at Uppsala University. I am also thankful to Dr. Anna Delin of KTH for useful discussions. I am thankful to my colleagues Oscar, Fredrik, Franchesko and Diana at Angstrom Laboratory, Uppsala.

I would like to thank seniors in my group D Paudyal, K K Saha, M Chakraborty and M Kabir for their continuous help. I would like to thank my collaborators at this centre Manoranjan and Soumendu. I enjoyed the company of my colleagues Kartick, Sourav, Tuhin, Roby, Moshior, Rudra, Mitali, Shreemoyee, Hena, Swastika, Prashant, Abhinav, Rajib, Hemant, Soumyajit, Kapil, Ambika, and Abhijit.

I acknowledge the financial support from S N Bose National Centre for Basic Sciences. I would like to thank all the academic and non-academic staffs at this centre for their cooperation in various ways.

As a part of my research work I have used the following packages whose originators I acknowledge with thanks : XCRYSDEN and Xmgrace softwares for drawing pictures.

While I stayed far away from home the encouragement and blessings of my parents were always with me. They deserve special thanks. All my family members and relatives, and in particular my wife Urmila encouraged me to pursue research study. I am thankful to all of them. At last I would like to thank my daughter Sneha whose appeal to come soon whenever I departed from home worked as a source of inspiration.

Manoj Kumar Yadav
Sapahi-9, Dhanusha, Nepal
September, 2009.

List of Publications

- 1. Band-gap variation in Mg- and Cd-doped ZnO nanostructures and molecular clusters.**
Manoj K Yadav, Manoranjan Ghosh, Ranjit Biswas, Arup K Raychaudhuri, Abhijit Mookerjee and Soumendu Datta.
Phys. Rev. B 76 (2007) p. 195450
- 2. Structural, electronic and magnetic properties of Cr-doped (ZnTe)₁₂ clusters.**
Manoj K Yadav, Biplab Sanyal and Abhijit Mookerjee.
J. Magn. Magn. Mater. 321 (2009) p. 235-240
- 3. Stabilization of ferromagnetism in Mn doped ZnO with C co-doping.**
Manoj K Yadav, Biplab Sanyal and Abhijit Mookerjee.
J. Magn. Magn. Mater. 321 (2009) p. 273-276
- 4. Tuning ferromagnetism in MnO.**
Manoj K Yadav, Biplab Sanyal and Abhijit Mookerjee.
J. Magn. Magn. Mater. (accepted)
- 5. Study of the electronic and structural properties of ZnO clusters.**
Manoj K Yadav, Biplab Sanyal and Abhijit Mookerjee.
Int. J. Mod. Phys. B (in press)
- 6. Magnetic properties of transition metal adsorbed zigzag graphene nanoribbon.**
Manoj K Yadav, Biplab Sanyal and Abhijit Mookerjee. (submitted)
- 7. Magnetic properties of transition metal doped MgO clusters.**
Manoj K Yadav, Biplab Sanyal and Abhijit Mookerjee. (manuscript)
- 8. On the validity of Rayleigh-Gans-Debye type approximations in red blood cell size determination.**
Manoj K Yadav and Subodh K Sharma.
J. Mod. Opt. 55 (2008) p. 921

⁰The contents of the papers with serial number 6 to 10 are not included in this thesis.

9. **Light propagation through fractal tissue: a critical study of phase function.**

S. K. Sharma, Srilekha Banerjee and M K Yadav.

J. Opt. A: Pure and applied optics 9 (2007) p. 49-55

10. **Dinitrogen dissociation on tantalum clusters.**

Manoj K Yadav and Abhijit Mookerjee. (manuscript)

Contents

1	Introduction	1
2	Theoretical background for electronic structure calculations	5
2.1	The electronic structure of solids as a many-body problem	5
2.2	Born-Oppenheimer Approximation	6
2.3	Density Functional Theory	7
2.3.1	The Hohenberg-Kohn Theorems	8
2.4	Approximations to Exchange-Correlation Functional	13
2.4.1	Local Density Approximation	14
2.4.2	Generalized Gradient Approximation	16
2.5	Plane Waves and Pseudopotentials	17
2.5.1	Plane Waves	17
2.5.2	Pseudopotentials	19
2.6	Projector Augmented Wave Method	21
2.7	Comments	23
3	Electronic and geometric properties of pristine ZnO clusters	24
3.1	Introduction	24
3.2	Methodology	25
3.3	Results and Discussion	27
3.4	Summary and Remarks	35
3.5	Comments	35
4	Tailoring the band gap of ZnO by doping	36
4.1	Introduction	36
4.2	Experimental Study	38
4.2.1	Synthesis	39
4.2.2	Characterization	40
4.2.3	Results and Analysis	41

4.2.4	Doped ZnO clusters	42
4.3	Summary	46
5	Magnetism in Cr doped ZnTe clusters	47
5.1	Introduction	47
5.2	Computational Details	49
5.3	Results and Discussion	49
5.3.1	Pristine (ZnTe) ₁₂ clusters	49
5.3.2	Monodoped clusters	51
5.3.3	Bi-doped clusters	53
5.4	Summary	58
6	Ferromagnetism in Mn doped and C co-doped ZnO	59
6.1	Introduction	59
6.2	Computational Details	60
6.3	Results and Discussion	61
6.4	Summary	65
7	Tuning ferromagnetism in manganese oxide	66
7.1	Introduction	66
7.2	Computational Details	67
7.3	Results and Discussion	68
7.4	Summary	72
8	Conclusion	74

List of Figures

3.1	(ZnO) _n clusters for n=2 to 7; large light spheres represent Zn atoms and smaller darker (red) spheres the O atoms. The subscripts <i>g</i> and <i>l</i> stand for global and local minima structures respectively.	28
3.2	(ZnO) _n clusters for n =8 to 12; large spheres represent Zn atoms and smaller spheres the O atoms. The subscripts <i>g</i> and <i>l</i> stand for global and local minima structures respectively.	30
3.3	The average Zn-O distance as a function of size of clusters.	33
3.4	(Left) Binding energy per ZnO unit versus size of cluster <i>n</i> . The circles are results of this work, while the dotted line represents the fitted function (3.3). (Right) Second difference in binding energy versus size of clusters <i>n</i>	33
3.5	(Left) HOMO-LUMO gap versus size of clusters <i>n</i> . (Right) Energy difference between ground states and the corresponding next higher energy isomers.	34
4.1	TEM images of (Left) undoped ZnO nano-structures, (Middle) Mg doped ZnO nano-structures and (Right) Cd doped ZnO nano-structures.	39
4.2	Absorption spectra of the nano-structures: (Left) Mg-doped nano-structure and (Right) Cd-doped nano-structure.	40
4.3	Ground state structures of (Left) (ZnO) ₉ and (Right) (ZnO) ₁₂ clusters. Large light (grey) spheres represent Zn atoms and smaller dark (red) spheres the O atoms.	42
4.4	Structures of (Left) Mg-doped (ZnO) ₁₂ cluster and (Right) Cd-doped (ZnO) ₁₂ cluster. Large light (grey) spheres represent Zn atoms and smaller darker (red) spheres the O atoms. The dopant atoms (Mg or Cd) are shown as large darker (blue) spheres.	43

4.5	(Left) Variation of the binding energy with Mg and Cd doping. (Middle) Variation in energy gaps with doping for $(\text{ZnO})_n$ clusters for $n=9$ and 12 . (Right) Comparison of theoretically obtained energy gaps in doped $(\text{ZnO})_{12}$ cluster with experimental energy gaps in doped nanostructures. The dotted lines are for convenience of visualization.	44
4.6	Charge densities (Left) pristine ZnO, (Middle) Mg doped ZnO, and (Right) Cd doped ZnO for (Top) $(\text{ZnO})_3$ ring and (Bottom) $(\text{ZnO})_2$ ring.	45
5.1	Ground state (GS) and local minima (LM1 and LM2) structures of pristine $(\text{ZnTe})_{12}$ clusters. White spheres represent Zn atoms and darker spheres represent Te atoms.	50
5.2	Optimized structures of mono-doped clusters, (Left to Right) M1, M2, M3 and M4. Dopant Cr atoms are represented by black spheres and colour codes of Zn and Te atoms are same as in Fig. 5.1.	51
5.3	Optimized structures of bi-doped $(\text{ZnTe})_{12}$ clusters: (Top) BF1, BF2 and BF3 (Bottom) BAF1, BAF2 and BAF3. Colour codes of atoms are the same as in Fig. 5.2. The parallel and antiparallel arrows indicate FM and AFM couplings respectively.	54
5.4	(Left) Total DOS of undoped $(\text{ZnTe})_{12}$ cluster and (Right) atom projected partial DOS of Cr- d and Te- p states of the mono-doped $(\text{ZnTe})_{12}$ cluster, M1. The dashed vertical line is the Fermi level (shifted to 0 eV). Majority (up) spin states are plotted along positive y axis and minority (down) spin states along negative y axis.	56
5.5	Partial DOS of Cr $3d$ and Te $5p$ states in the cluster BF1. Total DOS is also plotted which is scaled down for the sake of clarity. The dashed vertical line is the Fermi level (shifted to 0 eV). Majority (up) spin states are plotted along positive y axis and minority (down) spin states along negative y axis.	57
6.1	A portion of the 72-atom super-cell showing Mn and C doping sites. Three different C doping sites are marked as 1, 2 and 3.	62
6.2	Density of states of Mn- d and O- p for the AFM state of Mn doped ZnO. The dashed vertical line indicates the position of the Fermi levels (shifted to 0 eV). Majority (up) spin states are plotted along positive y axis and minority (down) spin states along negative y axis.	64

6.3	DOS of Mn- <i>d</i> and C- <i>p</i> for the FM state of carbon co-doped ZnMnO. The dashed vertical line indicates the position of the Fermi level (shifted to 0 eV).	65
7.1	Type II AFM ordering in MnO. Red spheres represent spin up Mn atoms and blue spheres spin down Mn atoms. Small white spheres represent O atoms.	68
7.2	Energy difference between ferromagnetic and anti-ferromagnetic Mn-Mn couplings as a function of doping concentration.	69
7.3	Density of states of pure MnO in type II AFM state. The dashed vertical line indicates the Fermi level (shifted to 0 eV). The total DOSs have been scaled down for the sake of clarity. Majority (up) spin states are plotted along positive y axis and minority (down) spin states along negative y axis.	71
7.4	Density of states of 12.5 at. % doped MnO in FM state. (Left) N doped and (Right) C doped. The total DOSs have been scaled down for the sake of clarity. The dashed vertical lines indicate the Fermi levels (shifted to 0 eV). Majority (up) spin states are plotted along positive y axis and minority (down) spin states along negative y axis.	72

List of Tables

3.1	The table shows a summary of the energetics and bond lengths for $(\text{ZnO})_n$ clusters with $n=2, \dots, 12$	32
5.1	Binding energy per atom, E_b in eV, formation energy, E_{form} in eV, HOMO-LUMO gap (smallest of the two spin channels), E_{gap} in eV and magnetic moments in Bohr-magneton (μ_B) of the mono-doped clusters.	52
5.2	Distance between Cr atoms, $d_{\text{Cr-Cr}}$ in Å, energy difference with respect to BF1, ΔE in eV, binding energy, E_b in eV/atom, and magnetic moments in units of Bohr-magneton (μ_B).	55
6.1	Relative energy ΔE in eV, Magnetic moment of Mn in μ_B , distance between Mn atoms, $d_{\text{Mn-Mn}}$ in Å, and distance between Mn and C atoms, $d_{\text{Mn-C}}$ in Å for configurations 1 , 2 and 3	63
7.1	Magnetic moments (in μ_B) on Mn, X (X= C and N) and O for FM and AFM configurations at 12.5 at. % doping.	70

Chapter 1

Introduction

I have never met a man so ignorant that I couldn't learn something from him.

-Galileo Galilei

Semiconductors, once considered to be dirty systems, today lie at the foundation of modern information technology. Presently the processing and communication of information is carried out by utilizing the charge of electrons in semiconductors while the mass storage of information is carried out by utilizing spin of electrons in ferromagnetic materials. Extensive research effort is on to combine these two in a single unit so that both charge and spin of electrons can be utilized simultaneously. This has led to the birth of new branch of semiconductor physics known as “spintronics”. With the realization of spintronic based devices the processing performance is expected to enhance largely. Furthermore, it may be possible to control spin state of electrons by injecting spin polarized current into the spintronic material which will be helpful in quantum computation.

The prerequisite for a spintronic material is that it has to be a ferromagnetic semiconductor. The conventional semiconductors like Si and GaAs are nonmagnetic semiconductors. There are some natural ferromagnetic semiconductors like europium chalcogenides and some semiconducting spinels. However, their crystal structures are incompatible with the crystal structures of Si or GaAs. Moreover, the crystal growth of these compounds

is extremely difficult. The next choice to achieve a suitable ferromagnetic semiconductor is to dope a semiconductor by some suitable magnetic element. Such a semiconductor is commonly known as diluted magnetic semiconductor (DMS). The theoretical prediction of the occurrence of ferromagnetism in wide band gap semiconductors like GaAs and ZnO prompted extensive research in this direction. The radiation insensitivity, low noise capability, high temperature and high frequency operation capability of these wide band gap materials offer extra advantages.

Ferromagnetism has been found in many materials like Mn doped GaAs, InAs and InSb. However, the transition temperature in these systems is well below the room temperature. This is the main hurdle for practical realization of these materials. While the initial DMS perspective research was focused to transition metal (TM) doped III-V semiconductors, recently II-VI semiconductor like ZnO has attracted much attention as it is easier to synthesize ZnO single crystal. Moreover, ZnO is more abundant and is more cost effective.

The aim of this thesis is to understand the structural, electronic and magnetic properties of wide band gap semiconductors employing the first principle density functional theory based calculations. The understanding of these properties is important from basic physical understanding viewpoint as well as for prospective application of such semiconductors in functional devices. The present study covers two size regimes of the wide band gap semiconductors: molecular clusters and bulk.

As clusters bridge the gap between molecules and the bulk material, their study is important for understanding the evolution of properties of materials when one goes from molecule to bulk. Clusters often exhibit novel properties. For example, the clusters of non magnetic elements are found to exhibit magnetism and clusters of metallic elements show the energy gap between the highest occupied molecular orbital (HOMO) and the lowest unoccupied molecular orbital (LUMO). Likewise their growth pattern is different from corresponding bulk. Moreover, these properties are found to vary remarkably with

the size and composition of the clusters and hence a cluster of desirable property can be synthesized by controlling these parameters. After the synthesis of fullerenes into fullerite (fullerene assembled solid), clusters are thought to be potential candidates for making cluster assembled solid. The synthesis of cluster assembled solid is expected to bring revolution in device miniaturization.

We have attempted to study structural and electronic properties of undoped and doped clusters of ZnO (Chapters 3 and 4). As the band gap engineering of ZnO is important for the development of devices like UV-blue light emitting diodes, visible blind UV photo detectors, quantum well structures and spintronic systems, we have paid particular attention to band gap (HOMO-LUMO gap for clusters) property of undoped and doped clusters of ZnO. In the regime of clusters the variation of size itself leads to variation in HOMO-LUMO gap. We have also shown that the HOMO -LUMO gap of a particular sized cluster can be tailored by doping with elements like Mg and Cd. The variation of HOMO-LUMO gap in Mg/Cd doped ZnO clusters is found to follow the similar trend as the variation of Mg/Cd doped bulk ZnO, and therefore, the theoretical results on clusters can be helpful for qualitative understanding of band gap variation in bulk.

Chapter 5 deals with the magnetic properties of Cr doped ZnTe clusters. A $(\text{ZnTe})_{12}$ cluster doped with single Cr atom exhibits atomic like magnetic moment unlike in the case of bulk where the moment of Cr atom gets reduced. The nature of magnetic coupling between two Cr atoms is found to depend on local environment, however the most stable structure exhibit ferromagnetic coupling. Moreover, Cr doping enhances the stability of clusters. These properties favor Cr doped ZnTe cluster to be a promising material for spintronic based devices.

The bulk systems studied are ZnMnO and MnO (Chapters 6 and 7). The occurrence of ferromagnetism in these wide band gap semiconductors is crucial for their spintronic applications. The experimental reports regarding the nature of magnetic coupling between Mn atoms in Mn doped ZnO are controversial. Some reports suggest occurrence

of even room temperature ferromagnetism while others suggest the occurrence of antiferromagnetic coupling. The results based on first principles calculations, however, suggest antiferromagnetic coupling to be the most stable state. We have shown that ferromagnetic state can be stabilized by co-doping ZnMnO with few concentration of carbon atom. The carbon substitution at O sites creates hole carriers into the system which lead to stabilization of ferromagnetic state. We apply similar hole doping trick to tune ferromagnetic coupling in an otherwise anti-ferromagnetic MnO. We have carried out substitutional doping at O sites of MnO by $2p$ elements like carbon and nitrogen. Such doping provides holes into the system which play role in stabilizing ferromagnetic ordering in MnO.

We should mention here that the idea of carrying out first-principle calculations is *not* simply to reproduce experimental data. That would be a pointless exercise. The idea would be to gain microscopic insight into why the data are as they are, why their trends in behaviour behave as they do. The ultimate aim would be to predict the behaviour of systems where experiments have not yet been carried out. This would help the experimentalist to both choosing material and designing experiments appropriately.

Chapter 2

Theoretical background for electronic structure calculations

2.1 The electronic structure of solids as a many-body problem

We shall model a solid as a collection of M ion-cores consisting of the nuclei and the tight-bound atomic like core electrons glued together with N valence electrons. The information about the behaviour of such system is contained in the many-body wave function $\psi(\mathbf{r}_1, \dots, \mathbf{r}_N; \mathbf{R}_1, \dots, \mathbf{R}_M)$ which is a function of all the ionic and electronic coordinates denoted by \mathbf{R}_α and \mathbf{r}_i respectively. The first principles, or *ab initio* calculation involves solution of the Schrödinger equation involving this wave-function :

$$\widehat{H}\psi(\mathbf{r}_1, \dots, \mathbf{r}_N; \mathbf{R}_1, \dots, \mathbf{R}_M) = E \psi(\mathbf{r}_1, \dots, \mathbf{r}_N; \mathbf{R}_1, \dots, \mathbf{R}_M) \quad (2.1)$$

where \widehat{H} is the many body Hamiltonian operator and E is the total energy of the system. The Hamiltonian operator describes the motion of all the ions and electrons in the system. If the motion of ions and electrons are treated in non-relativistic manner then in atomic units the Hamiltonian has the form:

$$\widehat{H} = - \sum_{\alpha=1}^M \frac{1}{2M_\alpha} \nabla_\alpha^2 - \sum_{i=1}^N \frac{1}{2} \nabla_i^2 - \sum_{\alpha=1}^M \sum_{i=1}^N \frac{Z_\alpha}{|\mathbf{r}_i - \mathbf{R}_\alpha|} + \sum_{i=1}^N \sum_{j>i}^N \frac{1}{|\mathbf{r}_i - \mathbf{r}_j|} + \sum_{\alpha=1}^M \sum_{\beta>\alpha}^M \frac{Z_\alpha Z_\beta}{|\mathbf{R}_\alpha - \mathbf{R}_\beta|} \quad (2.2)$$

where M_α is the ratio of mass of an ion-core to the mass of an electron and Z_α is the atomic number of α^{th} ion-core. The first term on the right of Eqn. (2.2) is the operator for kinetic energy of ion-cores, the second term is the operator for kinetic energy of electrons, the third term represents the Coulomb attraction between ion-cores and electrons, the fourth term represents the Coulomb repulsion between electrons and the last term represents the Coulomb repulsion between ion-cores.

2.2 Born-Oppenheimer Approximation

The third term on the right of Eqn. (2.2) couples the electronic coordinates with ion-core coordinates and hence poses a hurdle in separating the full Hamiltonian in terms of the ion-core and electronic Hamiltonians. This hurdle is overcome under Born-Oppenheimer Approximation [1] which assumes ion-cores to be fixed with respect to motion of electrons. The approximation is based on the fact that, in general, mass of an ion-core is much heavier than that of an electron and hence it moves so slowly with respect to an electron that it can be assumed to be stationary with respect to electronic motion. Within this approximation, for electronic motion, the first term on the right of Eqn. (2.2) can be neglected and the last term can be considered to be a constant which can be left while solving the Schrödinger equation for electrons and can be added later. Thus we are left with the electronic Hamiltonian:

$$\begin{aligned}\widehat{H}_{\text{elec}} &= -\frac{1}{2} \sum_i^N \nabla_i^2 + \sum_{i=1}^N \sum_{j>i}^N \frac{1}{|\mathbf{r}_i - \mathbf{r}_j|} - \sum_{\alpha=1}^M \sum_{i=1}^N \frac{Z_\alpha}{|\mathbf{r}_i - \mathbf{R}_\alpha|} \\ &= \widehat{T} + \widehat{V}_{ee} + \widehat{V}_{ext}\end{aligned}\tag{2.3}$$

The operators \widehat{T} and \widehat{V}_{ee} are the same for any system and hence they are universal operators. The system dependent information is entirely given by \widehat{V}_{ext} . The usual approach for calculating observables via the solution of the Schrödinger equation can be

summarized by the sequence:

$$\widehat{V}_{ext} \implies \psi(\mathbf{r}_1, \mathbf{r}_2, \dots, \mathbf{r}_N) \xrightarrow{\langle \psi | \hat{O} | \psi \rangle} \text{observables}$$

i.e., one first specifies the system by choosing \widehat{V}_{ext} , then solves the Schrödinger equation for the wave function ψ , and then observables are computed by taking the expectation values of the corresponding operators with this wave function ψ . For example the electron density can be calculated as

$$\rho(\mathbf{r}) = N \int \dots \int |\psi(\mathbf{r}, \mathbf{r}_2, \mathbf{r}_3, \dots, \mathbf{r}_N)|^2 d\mathbf{r}_2 d\mathbf{r}_3 \dots d\mathbf{r}_N \quad (2.4)$$

The Born-Oppenheimer approximation does simplify the Schrödinger equation, but it is still a formidable problem when one deals with many electron system. The methods like configuration interactions and diagrammatic perturbation theory are successful in dealing with systems with few electrons, but they are computationally intractable for large clusters of atoms and impossible for solids where there are $\sim 10^{20}$ valence electrons.

The breakthrough in tackling this problem came with the advent of Density Functional Theory (DFT) which is discussed briefly in the following section.

2.3 Density Functional Theory

In late 1920's Thomas [2] and Fermi [3] introduced the idea of expressing the total energy of a system as a functional of the total electron density. Since then this idea of using electron density as a variable to express the energy of a system has undergone various stages of developments. The real breakthrough was brought about by the Hohenberg-Kohn's two theorems [4] and later by the variational formulation of the Kohn-Sham equation [5]. Presently DFT is considered to be one of the most successful quantum mechanical methods in tackling many body problem where 'strong correlation' is not an issue. The importance of DFT can be emphasized by the fact that Kohn, one of its developers, and

Pople, who played instrumental role in implementing DFT in computational chemistry were awarded by the Nobel prize in 1998.

2.3.1 The Hohenberg-Kohn Theorems

In 1964 Hohenberg and Kohn proved two theorems [4]. Their first theorem showed that the ground state electron density $\rho_o(\mathbf{r})$ of a system of interacting electrons in some external potential $v(\mathbf{r})$ determines this potential up to an additive constant. The implication of Hohenberg Kohn theorem is that since $v(\mathbf{r})$ fixes H so does $\rho_o(\mathbf{r})$ and hence the ground state wave function ψ_o becomes unique functional of the ground state electron density $\rho_o(\mathbf{r})$. Thus, any observable O of a system in ground state also becomes functional of $\rho_o(\mathbf{r})$ and can be calculated by finding the expectation value of the corresponding operator with the ground state wave function.

$$O = O[\rho_o(\mathbf{r})] = \langle \psi[\rho_o(\mathbf{r})] | \hat{O} | \psi[\rho_o(\mathbf{r})] \rangle \quad (2.5)$$

For example, the ground state energy of the system can be calculated as

$$E_o = E[\rho_o(\mathbf{r})] = \langle \psi[\rho_o(\mathbf{r})] | H | \psi[\rho_o(\mathbf{r})] \rangle$$

Since ground state energy is a function of a number of parameters of the system, it can be used to calculate the respective ground state properties by minimizing the ground state energy with respect to these parameters.

For a given electron density $\rho(r)$, the total energy can be cast explicitly in terms of functional forms of the individual terms in the Hamiltonian as

$$E[\rho(\mathbf{r})] = T[\rho(\mathbf{r})] + V_{ee}[\rho(\mathbf{r})] + V_{ext}[\rho(\mathbf{r})], \quad (2.6)$$

where $T[\rho(\mathbf{r})]$ and $V_{ee}[\rho(\mathbf{r})]$ are universal functionals [independent of $v(\mathbf{r})$] and can be found using Eqn. (2.5). The last term in Eqn. (2.6) is system dependent and can be

found as

$$V_{ext}[\rho(\mathbf{r})] = \int d\mathbf{r} \rho(\mathbf{r})v(\mathbf{r}) \quad (2.7)$$

The second Hohenberg-Kohn theorem establishes the variational principle. The ground state energy and density correspond to the minimum of some functional $E[\rho(r)]$ subject to the constraint that the density contains the correct number of electrons in the system.

$$\delta \left\{ E[\rho(\mathbf{r})] - \mu \left(\int \rho(\mathbf{r})d\mathbf{r} - N \right) \right\} = 0, \quad (2.8)$$

where the Lagrange's multiplier μ is the electronic chemical potential. This implies that given any trial density $\rho_t(\mathbf{r})$ of a system of N electrons in an external potential $v(\mathbf{r})$, the total energy calculated with this density will always be greater than or equal to the ground state energy E_o .

$$T[\rho_t(\mathbf{r})] + V_{ext}[\rho_t(\mathbf{r})] + V_{ee}[\rho_t(\mathbf{r})] = E[\rho_t(\mathbf{r})] \geq E_o \quad (2.9)$$

The equality sign holds only for the ground state density $\rho_o(\mathbf{r})$. Thus, the ground state energy of the system can be retrieved by minimizing Eqn. (2.6) with respect to $\rho(\mathbf{r})$. The function that minimizes the energy is the ground state density $\rho_o(r)$ and the corresponding energy is the ground state energy.

However, there are practical difficulties in this minimization scheme. First of all, one does not know the exact form of the functionals $T[\rho(\mathbf{r})]$ and $V_{ee}[\rho(\mathbf{r})]$. One can split $V_{ee}[\rho(\mathbf{r})]$ into classical and non-classical parts. The classical part is just the Hartree energy. Still the functional forms of kinetic energy term and non-classical part of potential energy remain unknown. So, to start with we need reliable approximations for them. Second, the minimization of $E[\rho_t(\mathbf{r})]$ is a tough numerical problem on its own.

One may try to express kinetic and potential energy terms in terms of first and second order density matrices $\gamma_1(\mathbf{x}'_1, \mathbf{x}_1)$ and $\gamma_2(\mathbf{x}'_1, \mathbf{x}'_2; \mathbf{x}_1, \mathbf{x}_2)$. These density matrices are defined as

$$\gamma_1(\mathbf{x}'_1, \mathbf{x}_1) = N \int \dots \int \psi^*(\mathbf{x}'_1, \mathbf{x}_2 \dots \mathbf{r}_N) \psi(\mathbf{x}_1, \mathbf{x}_2 \dots \mathbf{x}_N) d\mathbf{x}_2 \dots d\mathbf{x}_N \quad (2.10)$$

$$\begin{aligned} \gamma_2(\mathbf{x}'_1, \mathbf{x}'_2; \mathbf{x}_1, \mathbf{x}_2) &= \frac{N(N-1)}{2} \\ &\int \dots \int \psi(\mathbf{x}'_1, \mathbf{x}'_2, \mathbf{x}_3, \dots \mathbf{x}_N) \psi^*(\mathbf{x}_1, \mathbf{x}_2, \mathbf{x}_3, \dots \mathbf{x}_N) d\mathbf{x}_3 \dots d\mathbf{x}_N \end{aligned} \quad (2.11)$$

The summation over spin coordinates results the spinless density matrices. The first and second order spinless density matrices are given by

$$\rho_1(\mathbf{r}'_1, \mathbf{r}_1) = \int \gamma_1(\mathbf{r}'_1 s_1, \mathbf{r}_1 s_1) ds_1 \quad (2.12)$$

$$\rho_2(\mathbf{r}'_1, \mathbf{r}'_2; \mathbf{r}_1, \mathbf{r}_2) = \int \int \gamma_2(\mathbf{r}'_1 s_1, \mathbf{r}'_2 s_2) ds_1 ds_2 \quad (2.13)$$

The diagonal elements of $\rho_1(\mathbf{r}'_1, \mathbf{r}_1)$ is just the electron density

$$\begin{aligned} \rho(\mathbf{r}_1) &= \rho_1(\mathbf{r}_1, \mathbf{r}_1) \\ &= N \int \dots \int |\Psi|^2 ds_1 d\mathbf{x}_2 \dots d\mathbf{x}_N \end{aligned} \quad (2.14)$$

The diagonal elements of $\rho_2(\mathbf{r}'_1, \mathbf{r}'_2; \mathbf{r}_1, \mathbf{r}_2)$ gives the electron pair density

$$\begin{aligned} \rho_2(\mathbf{r}_1, \mathbf{r}_2) &= \rho_2(\mathbf{r}_1, \mathbf{r}_2; \mathbf{r}_1, \mathbf{r}_2) \\ &= \frac{N(N-1)}{2} \int \dots \int |\Psi|^2 ds_1 ds_2 d\mathbf{x}_3 \dots d\mathbf{x}_N \end{aligned} \quad (2.15)$$

One particle density and two particle density (the pair density) are related by the expression

$$\rho(\mathbf{r}_1) = \frac{2}{N-1} \int \rho_2(\mathbf{r}_1, \mathbf{r}_2) d\mathbf{r}_2 \quad (2.16)$$

The total energy functional can be expressed in terms of one and two particle densities as

$$\begin{aligned} E &= E[\rho_1(\mathbf{r}'_1, \mathbf{r}_1), \rho_2(\mathbf{r}_1, \mathbf{r}_2)] \\ &= \int \left[-\frac{1}{2} \nabla^2 \rho_1(\mathbf{r}', \mathbf{r}) \right]_{r'=r} d\mathbf{r} + \int v(\mathbf{r}) \rho(\mathbf{r}) d\mathbf{r} + \int \int \frac{1}{\mathbf{r}_{12}} \rho_2(\mathbf{r}_1, \mathbf{r}_2) d\mathbf{r}_1 d\mathbf{r}_2 \end{aligned} \quad (2.17)$$

The three terms on the right of Eqn. (2.17) represent kinetic energy, nuclear-electron potential energy and the electron-electron potential energy respectively. The last term

can be further simplified if we express $\rho_2(\mathbf{r}_1, \mathbf{r}_2)$ in terms of pair correlation function $h(\mathbf{r}_1, \mathbf{r}_2)$ as

$$\rho_2(\mathbf{r}_1, \mathbf{r}_2) = \frac{1}{2}\rho(\mathbf{r}_1)\rho(\mathbf{r}_2)[1 + h(\mathbf{r}_1, \mathbf{r}_2)] \quad (2.18)$$

Using Eqs. (2.16) and (2.18), we get

$$\frac{N-1}{2}\rho(\mathbf{r}_1) = \frac{1}{2}[N + \int \rho(\mathbf{r}_2)h(\mathbf{r}_1, \mathbf{r}_2)d\mathbf{r}_2] \quad (2.19)$$

The quantity $\rho(\mathbf{r}_2)h(\mathbf{r}_1, \mathbf{r}_2) = \rho_{xc}(\mathbf{r}_1, \mathbf{r}_2)$ is known as exchange correlation hole. It integrates to -1; i.e.

$$\int \rho_{xc}(\mathbf{r}_1, \mathbf{r}_2)d\mathbf{r}_2 = -1 \quad (2.20)$$

The electron-electron potential energy term in Eqn. (2.17) can be expressed in terms of exchange correlation hole as

$$V_{ee} = \frac{1}{2} \int \int \frac{1}{r_{12}} \rho(\mathbf{r}_1)\rho(\mathbf{r}_2)d\mathbf{r}_1d\mathbf{r}_2 + \frac{1}{2} \int \int \frac{1}{r_{12}} \rho(\mathbf{r}_1)\rho_{xc}(\mathbf{r}_1, \mathbf{r}_2)d\mathbf{r}_1d\mathbf{r}_2 \quad (2.21)$$

Now one may try to minimize Eqn. (2.17) with respect to $\rho_2(\mathbf{r}_1, \mathbf{r}_2)$ (since $\rho(\mathbf{r}_1)$ is related with $\rho_2(\mathbf{r}_1, \mathbf{r}_2)$ via Eq. 2.16). This approach suffers a major obstacle with the requirement that $\rho_2(\mathbf{r}_1, \mathbf{r}_2)$ must correspond to some antisymmetric wave function. Although a formal solution of this N-representability problem exists, it does not lead to efficient minimization.

The problem is overcome by Kohn-sham approach [5]. in which the kinetic energy functional is decomposed into two parts:

$$T[\rho(\mathbf{r})] = T_s[\rho(\mathbf{r})] + T_c[\rho(\mathbf{r})], \quad (2.22)$$

where $T_s[\rho(\mathbf{r})]$, known as Kohn-Sham kinetic energy, represents the kinetic energy of non-interacting particles having the same density $\rho(\mathbf{r})$ as that of the original interacting particles and T_c represents the remainder of the kinetic energy arising due to the effect of interactions between them.

$T_s[\rho(\mathbf{r})]$ can be found exactly from Hartree-Fock theory:

$$T_s[\rho(\mathbf{r})] = -\frac{1}{2} \sum_i^N \langle \varphi_i(\mathbf{r}) | \nabla^2 | \varphi_i(\mathbf{r}) \rangle \quad (2.23)$$

where φ_i are one-electron orbitals (known as Kohn-Sham orbitals) for non-interacting system. Within this scheme the main part of total kinetic energy is calculated exactly. The energy functional of Eqn. (2.6) within Kohn-Sham approach can be written as:

$$E[\rho(\mathbf{r})] = T_s[\varphi_i[\rho(\mathbf{r})]] + V_H[\rho(\mathbf{r})] + E_{xc} + V_{ext}[\rho(\mathbf{r})], \quad (2.24)$$

where the Hartree energy, V_H represents the energy arising from classical Coulomb interaction. The non-classical parts of $T[\gamma_1]$ and $V_{ee}[\gamma_2]$ are included in E_{xc} , known as exchange correlation energy, i.e.

$$E_{xc}[\rho, \gamma_1, \gamma_2] = T[\gamma_1] - T_s[\rho] + V_{ee}[\gamma_2] - V_H[\rho]$$

The minimization condition for Eqn. (2.24) can be written as

$$\begin{aligned} \frac{\delta E[\rho(\mathbf{r})]}{\delta \rho(\mathbf{r})} = 0 &= \frac{\delta T_s[\rho(\mathbf{r})]}{\delta \rho(\mathbf{r})} + \frac{\delta V_{ext}[\rho(\mathbf{r})]}{\delta \rho(\mathbf{r})} + \frac{\delta V_H[\rho(\mathbf{r})]}{\delta \rho(\mathbf{r})} + \frac{\delta E_{xc}}{\delta \rho(\mathbf{r})} \\ &= \frac{\delta T_s[\rho(\mathbf{r})]}{\delta \rho(\mathbf{r})} + v(\mathbf{r}) + v_H(\mathbf{r}) + v_{xc}(\mathbf{r}), \end{aligned} \quad (2.25)$$

The minimization condition for a system of non interacting particles moving in the potential $v_s(\mathbf{r})$ can be written as:

$$\begin{aligned} \frac{\delta E[\rho(\mathbf{r})]}{\delta \rho(\mathbf{r})} = 0 &= \frac{\delta T_s[\rho(\mathbf{r})]}{\delta \rho(\mathbf{r})} + \frac{\delta V_s[\rho(\mathbf{r})]}{\delta \rho(\mathbf{r})} \\ &= \frac{\delta T_s[\rho(\mathbf{r})]}{\delta \rho(\mathbf{r})} + v_s(\mathbf{r}) \end{aligned} \quad (2.26)$$

Comparing Eqs. (2.25) and (2.26) we find that both minimization schemes yield the same solution $\rho_s(\mathbf{r}) \equiv \rho(\mathbf{r})$, if v_s is chosen to be

$$v_s(\mathbf{r}) = v(\mathbf{r}) + v_H(\mathbf{r}) + v_{xc}(\mathbf{r}) \quad (2.27)$$

The ‘Schrödinger-like’ Kohn-Sham equation for this auxiliary system in which electrons move in effective potential v_s can be written as

$$\left[-\frac{1}{2} \nabla^2 + v_s(\mathbf{r}) \right] \varphi_i = \epsilon_i \varphi_i(\mathbf{r}) \quad (2.28)$$

The solution of this equation yields orbitals that reproduce the density $\rho(\mathbf{r})$ of the original interacting system.

$$\rho(\mathbf{r}) \equiv \rho_s(\mathbf{r}) = \sum_i^N f_i |\varphi_i(\mathbf{r})|^2, \quad (2.29)$$

where f_i is the occupancy of the orbital. Equations (2.28) and (2.29) are celebrated Kohn-Sham equations. These equations are like single-particle Schrödinger equations, however the many body effects are still there in the form of exchange correlation functional. Because of these equations DFT became viable tool for studying macroscopic systems.

Since $v_s(\mathbf{r})$ depends on $\rho(\mathbf{r})$, and $\rho(\mathbf{r})$ depends on φ_i which are the solutions of the Kohn-Sham equation, Eqn. (2.29) has to be solved self consistently. One first starts with the initial guess for $\rho(\mathbf{r})$, calculates the corresponding $v_s(\mathbf{r})$, and then solves Eqn. (2.29) for φ_i . From these φ_i new density $\rho(\mathbf{r})$ is calculated and the process is repeated until convergence is achieved.

2.4 Approximations to Exchange-Correlation Functional

The calculation of $v_s(\mathbf{r})$ is not possible without the knowledge of the exchange correlation functional $v_{xc}(\mathbf{r})$ which contains all the many body effects. The explicit density functional

form of $v_{xc}(\mathbf{r})$ is not known and has to be approximated. The accuracy of DFT largely depends on the quality of the approximation for $v_{xc}(\mathbf{r})$.

2.4.1 Local Density Approximation

The simplest and remarkably successful approximation to $v_{xc}(\mathbf{r})$ is the local density approximation (LDA). In this approximation the exchange correlation energy is expressed in terms of exchange correlation energy of a homogeneous electron gas [5].

$$E_{xc}^{LDA}[\rho(\mathbf{r})] = \int \rho(\mathbf{r}) \varepsilon_{xc}(\rho(\mathbf{r})) d\mathbf{r}, \quad (2.30)$$

where $\varepsilon_{xc}(\rho(\mathbf{r}))$ is the exchange correlation energy per particle of a homogeneous electron gas of density $\rho(\mathbf{r})$, and can be decomposed into exchange and correlation contributions :

$$\varepsilon_{xc}(\rho(\mathbf{r})) = \varepsilon_x(\rho(\mathbf{r})) + \varepsilon_c(\rho(\mathbf{r}))$$

The expression for exchange part was derived by Bloch and Dirac:

$$\varepsilon_x(\rho(\mathbf{r})) = -\frac{3}{4} \left(\frac{3\rho(\mathbf{r})}{\pi} \right)^{1/3}$$

The functional form of correlation energy, ε_c is not known. Earlier approximate expressions for ε_c were based on perturbation theory. Now a days it is obtained in a parametrized form with the help of Quantum Monte Carlo (QMC) techniques.

In spite of this rather crude approximation, LDA is successful in reproducing accurate band structures and total energies for many systems. However, it has well known limitation of over binding the electrons in molecules due to which it predicts stability of some unstable molecules. One way to improve LDA is to incorporate electron's spin into it. This leads to the Local Spin Density Approximation (LSD) which can be expressed as

$$E_{xc}^{LSD}[\rho_{\uparrow}(\mathbf{r}), \rho_{\downarrow}(\mathbf{r})] = \int d\mathbf{r} \rho(\mathbf{r}) \varepsilon_{xc}(\rho_{\uparrow}(\mathbf{r}), \rho_{\downarrow}(\mathbf{r})), \quad (2.31)$$

where $\rho(\mathbf{r}) = \rho_{\uparrow}(\mathbf{r}) + \rho_{\downarrow}(\mathbf{r})$. As in the case of LDA, $\varepsilon(\rho_{\uparrow}(\mathbf{r}), \rho_{\downarrow}(\mathbf{r}))$ can be decomposed into exchange and correlation parts :

$$\varepsilon_{xc}(\rho_{\uparrow}(\mathbf{r}), \rho_{\downarrow}(\mathbf{r})) = \varepsilon_x(\rho_{\uparrow}, \rho_{\downarrow}) + \varepsilon_c(\rho_{\uparrow}, \rho_{\downarrow})$$

The exchange contribution comes from the electrons having similar spin and hence is dependent on spin polarization parameter

$$\xi = \frac{\rho_{\uparrow}(\mathbf{r}) - \rho_{\downarrow}(\mathbf{r})}{\rho(\mathbf{r})}$$

ξ attains the value of 1 for completely spin polarized system and 0 for fully spin compensated system. The exchange part of $\varepsilon_{xc}(\rho_{\uparrow}(\mathbf{r}), \rho_{\downarrow}(\mathbf{r}))$ is given by

$$\varepsilon_x(\rho_{\uparrow}, \rho_{\downarrow}) = \varepsilon_x(r_s, \xi) = \varepsilon_x^P(r_s) + [\varepsilon_x^F(r_s) - \varepsilon_x^P(r_s)] f(\xi), \quad (2.32)$$

where r_s is the radius of the effective sphere for an electron,

$$r_s = \left(\frac{3}{4\pi\rho(\mathbf{r})} \right)^{1/3}$$

The superscripts F and P in Eqn. (2.32) represents the fully spin polarized (ferromagnetic) and fully spin compensated (paramagnetic) cases respectively. The relations between the terms $\varepsilon_x^P(r_s)$ and $\varepsilon_x^F(r_s)$ is given by

$$\varepsilon_x^P(r_s) = 2^{-1/3} \varepsilon_x^F(r_s) = -\frac{3}{r_s} \left(\frac{9}{32\pi^2} \right) \quad (2.33)$$

The function $f(\xi)$ in Eqn. (2.32) is given by

$$f(\xi) = \frac{(1 + \xi)^{4/3} + (1 - \xi)^{4/3} - 2}{2(2^{1/3} - 1)}. \quad (2.34)$$

The excess correlation energy which results from the interactions between *all* electrons (unlike exchange energy) is given by

$$\varepsilon_c(\rho_\uparrow, \rho_\downarrow) = \int \rho(\mathbf{r}) \varepsilon_c(\rho(\mathbf{r}), \xi) d\mathbf{r}, \quad (2.35)$$

However, the precise form of $\varepsilon_c(\rho(\mathbf{r}), \xi)$ is not known. There are analytical expressions for limiting cases like low density limit [6] and high density limit [7, 8]. von Barth and Hedin [9] proposed an expression for $\varepsilon_c(\rho(\mathbf{r}), \xi)$ based on random phase approximation (RPA). The expression has similar form as of Eqn. (2.32):

$$\varepsilon_c^{BH}(\rho(\mathbf{r}), \xi) = \varepsilon_c^P(r_s) + [\varepsilon_c^F(r_s) - \varepsilon_c^P(r_s)] f(\xi), \quad (2.36)$$

A modified form of ε_c^{BH} has been proposed by Vosko, Wilk and Nusair [10]

$$\varepsilon_c^{VWN} = \varepsilon_c^P(r_s) + \alpha(r_s) \left[\frac{f(\xi)}{f''(0)} \right] [1 + \beta(r_s)\xi^4], \quad (2.37)$$

where $\alpha(r_s)$ is the spin stiffness, related to spin susceptibilities and $\beta(r_s)$ is adjusted to satisfy $\varepsilon_c(r_s, 1) = \varepsilon_c^F(r_s)$, i.e.

$$1 + \beta(r_s) = f''(0) \frac{\varepsilon_c^F(r_s) - \varepsilon_c^P(r_s)}{\alpha(r_s)} \quad (2.38)$$

ε_c^{VWN} usually enhances the magnetic moments and magnetic energies compared to ε_c^{BH} .

2.4.2 Generalized Gradient Approximation

The electron density in a real system is not uniform rather it is spatially varying. Thus, the inclusion of the gradient of density into the exchange correlation functional would clearly improve the accuracy. The functionals that include the gradients of the charge density are known as generalized gradient approximations (GGA). The form of GGA functional is given by

$$E_{xc}^{GGA} = \int f(\rho_\uparrow(\mathbf{r}), \rho_\downarrow(\mathbf{r}), \nabla\rho_\uparrow(\mathbf{r}), \nabla\rho_\downarrow(\mathbf{r})) d\mathbf{r}. \quad (2.39)$$

There exists different expressions for f proposed by different authors. The accuracy of GGA depends on the type of f used. The widely used GGAs are Perdew and Wang (PW91) [11], Perdew, Burke and Ernzerhof (PBE) [12] and BLYP which is a combination of Becke's 1988 exchange functional [13] and the 1988 correlation functional of Lee, Yang and Parr [14]. In this thesis we have mostly used PBE functional. It preserves all the requirements of LSDA. It is made to satisfy further physical constraints by incorporating the dependence on reduced density gradient $s = |\nabla \rho|/(2k_F \rho)$. Thus, PBE exchange correlation energy depend on ρ , s and ξ :

$$E_{XC}^{PBE} = \int d\mathbf{r} \rho(\mathbf{r}) (r_s(r), s(\mathbf{r}), \xi(\mathbf{r})). \quad (2.40)$$

2.5 Plane Waves and Pseudopotentials

In order to solve the Kohn-Sham equation, we expand Kohn-Sham orbitals in terms of a basis set. Within DFT framework plane wave pseudo-potential approach has been widely used for electronic structure calculations of large, many-atomic systems like clusters and solids. Plane wave basis expansion is mathematically simple and coupled with pseudo-potential approach the size of basis can be drastically reduced. The plane wave and pseudo-potential approaches are detailed in the following two sections.

2.5.1 Plane Waves

The expansion of the KS orbitals in a given basis leads to

$$\varphi_i(r) = \sum_{j=1} c_j \phi_j(\mathbf{r}), \quad (2.41)$$

where $\phi_j(\mathbf{r})$ are basis functions. Plane waves are suitable choice for basis functions $\phi_j(\mathbf{r})$. Plane waves are orthonormal and energy independent, and hence converts the KS equation to a simple matrix eigenvalue problem for the expansion coefficients. Plane waves are

unbiased, i.e. they are independent of any particular atom. They are also independent of atomic positions and hence the Hellmann-Feynman theorem can be directly applied to calculate forces on the ion-cores. These forces allow us to relax the structure and carry out molecular dynamics to ascertain the equilibrium structure. The electronic structure determination is carried out on the equilibrium structure, i.e. when the forces on all ion-cores are below a suitably small threshold value. The Pulay terms in the force calculations which arise because of changes in the basis themselves when the ion-cores move, are identically zero. These properties of the plane wave basis make it a popular choice for basis functions. Ideally the plane wave basis are applicable only to KS orbitals for periodic infinite solids for which the Bloch Theorem is valid, however, they can also be applied for the electronic structure calculations of point defects, surfaces, molecules and clusters by making use of periodic super-cell. The size of the super-cell should be large enough to avoid interaction between its periodic images.

The potential of a periodic system has the periodicity of the underlying lattice, i.e.

$$V(\mathbf{r} + \mathbf{R}) = V(\mathbf{r})$$

where \mathbf{R} is the Bravais lattice vector. According to Bloch's theorem, a wave function in a periodic potential can be expressed as

$$\varphi_j(\mathbf{r}) = u_{jn}(\mathbf{r}, \mathbf{k}) \exp^{i\mathbf{k}\cdot\mathbf{r}} \quad (2.42)$$

where n is the band index and \mathbf{k} is a vector confined to the first Brillouin zone. The function $u_{jn}(\mathbf{r}, \mathbf{k})$ is a periodic function having the same periodicity of the Bravais lattice. Therefore, it can be expanded as a set of plane waves:

$$u_{jn}(\mathbf{r}, \mathbf{k}) = \sum_{\mathbf{G}} c_{j,n,\mathbf{G}} \exp^{i\mathbf{G}\cdot\mathbf{r}}, \quad (2.43)$$

where \mathbf{G} is the reciprocal lattice vector. Using Eqs. (2.42) and (2.43) we arrive at

$$\varphi_{j,\mathbf{k}}(\mathbf{r}) = \sum_{\mathbf{G}} c_{j,\mathbf{k}+\mathbf{G}} e^{i(\mathbf{k}+\mathbf{G})\cdot\mathbf{r}} \quad (2.44)$$

In order to reproduce the actual wave function $\varphi_{j,\mathbf{k}}(\mathbf{r})$ an infinite number of basis functions in the expansion would be needed. However, in practice only a finite number of basis functions are taken for the sake of computational convenience. The number of basis functions is controlled by choosing a certain value for the wave vector in the expansion of Eqn. (2.44). This is equivalent to imposing a cut off on kinetic energy, as the kinetic energy of electron with wave-vector \mathbf{k} is proportional to $|\mathbf{k} + \mathbf{G}|^2$.

2.5.2 Pseudopotentials

Plane wave basis requires large number of basis functions to describe the wave functions close to nucleus. This is due to two reasons: first the wave function near to nucleus shows steep behavior and second the orthogonality requirements between the valence and core electron wave functions causes rapid oscillation of valence wave functions near the core region.

The problem can be simplified by the use of pseudo-potential approximation. Since the wave functions near the core is shielded from the outer region and most of properties of matter depend only upon valence wave functions, one can replace the potential in core region by a pseudo-potential. Pseudo-potential is designed to yield very smooth wave function (nodeless) in core region (thus requiring less number of plane waves) and the actual wave function outside the core region. Thus the chemically important valence electrons feel almost the same environment as before. This approximation drastically reduces the number of plane waves which can be managed on computers.

Pseudo-potentials are usually generated from all electron calculation for an atomic reference configuration. The all electron KS equation is solved self consistently under the framework of DFT. The solution of all electron KS equation

$$-\frac{1}{r^2} \frac{d^2}{dr^2} \left(r^2 \varphi_{iL}(r, \epsilon_L) \right) + \left[\frac{\ell(\ell+1)}{r^2} + V[\rho] - \epsilon_L \right] \varphi_{iL}(r, \epsilon_L) = 0, \quad (2.45)$$

where $L = (\ell, m)$ are the composite angular momentum indices, yields the self consistent potential V as well as the all-electron wave functions and energy eigenvalues. The resulting valence eigenvalues are substituted back into the KS equation, but with a parametrized pseudo wave-function. The KS equation is then inverted to get the pseudo-potential.

Pseudo-potentials must obey certain criteria :

- Outside the core region the pseudo wave function $\varphi_i^{ps}(r)$ must match the actual wave function $\varphi_i(r)$: $\varphi_i^{ps}(r) = \varphi_i(r)$ for $r > r_c$
- The pseudo wave function must be continuous at the cut off radius, and so must be its first and second derivatives : $\partial^m \varphi_i^{ps}(r_c) / \partial r^m = \partial^m \varphi_i(r_c) / \partial r^m$ for $m=0,1,2$.
- The valence all-electron and pseudo-potential eigen values must be equal : $\epsilon_i^{ps} = \epsilon_i$

Apart from these a good pseudo-potential must be soft and transferable. A pseudo-potential is soft if it requires less number of plane waves. A pseudopotential is transferable if it works reasonably well in different environments.

Norm conserving pseudo-potential (NCP) [15, 16] are constructed with an extra constraint that the pseudo wave function must preserve the charge density inside the core region :

$$\int_0^{r_c} |\varphi_i^{ps}(r)|^2 r^2 dr = \int_0^{r_c} |\varphi_i(r)|^2 r^2 dr \quad (2.46)$$

NCP works well for most elements except for some first period $2p$ and $3d$ elements. In these cases norm conserving pseudo wave-functions are not significantly smoother than the all-electron wave function. For these elements a large energy cut off is required to obtain desirable results. To make pseudo wave-function softer r_c has to be increased

which decreases transferability. Thus one has to make a compromise between softness and transferability.

The norm conserving condition forces the wave function to vary rapidly thus requiring larger basis set. To get rid of this problem Vanderbilt [17] developed a new pseudo-potential by relaxing the norm conservation constraint. Such pseudo-potential requires much less number of plane waves and hence known as ultra-soft pseudo-potential.

2.6 Projector Augmented Wave Method

The projector augmented wave (PAW) method [18, 19] is an all-electron method. The usual pseudo-potential method has two main drawbacks: requirement of large basis set for the accurate description of bonding and tail region, and lack of good description of nodal structure of the wave function near the core region. PAW method overcomes these problems by using the wave function which is combination of pseudo wave function and expansions of atomic and pseudo atomic orbital terms.

PAW method uses a linear transformation τ that maps the true all-electron wave functions $|\psi_n\rangle$ with their nodal structure on to smooth auxiliary wave functions $|\tilde{\psi}_n\rangle$.

$$|\psi_n\rangle = \tau|\tilde{\psi}_n\rangle, \quad (2.47)$$

Inside augmentation region ($|\mathbf{r} - \mathbf{R}| < r_c$), true and auxiliary wave function can be expanded in terms of respective partial waves,

$$\psi = \sum_i c_i |\phi_i\rangle, \quad \tilde{\psi} = \sum_i c_i |\tilde{\phi}_i\rangle$$

where i is a composite index referring to the atomic site \mathbf{R} , the \mathbf{k} index and the quantum numbers ℓ and m . The coefficients in these expansions are given by

$$c_i = \langle \tilde{p}_i | \tilde{\psi} \rangle$$

where $\langle \tilde{p}_i |$ are projector functions. Inside the augmentation region the projector functions satisfy the relations

$$\sum_i |\tilde{\phi}_i\rangle \langle \tilde{p}_i| = 1, \quad \langle \tilde{p}_i | \tilde{\phi}_j \rangle = \delta_{ij}$$

The operator τ has to modify the auxiliary wave function in the augmentation region to reproduce the correct nodal structure. Outside the augmentation region it should not change the auxiliary wave function. Thus, the proper expression for τ is

$$\tau = 1 + \sum_i (|\phi_i\rangle - |\tilde{\phi}_i\rangle) \langle \tilde{p}_i| \quad (2.48)$$

where the sum runs over all partial waves of all atoms. Using Eqs. (2.47) and (2.48), the true wave function can be expressed as

$$|\psi\rangle = |\tilde{\psi}\rangle + \sum_i (|\phi_i\rangle - |\tilde{\phi}_i\rangle) \langle \tilde{p}_i | \tilde{\psi}\rangle$$

The expectation values can be obtained either from the true wave function or from auxiliary wave functions

$$\langle A \rangle = \sum_n f_n \langle \psi_n | A | \psi_n \rangle + \sum_{n=1}^{N_c} \langle \phi_n^c | A | \phi_n^c \rangle = \sum_n f_n \langle \tilde{\psi}_n | \tau^\dagger A \tau | \tilde{\psi}_n \rangle + \sum_{n=1}^{N_c} \langle \phi_n^c | A | \phi_n^c \rangle \quad (2.49)$$

where f_n are the occupancies of the valence states and N_c is the number of core states.

Using Eqn. (2.49) the all-electron charge density in PAW method is given by

$$\rho(\mathbf{r}) = \tilde{\rho}(\mathbf{r}) + \rho^1(\mathbf{r}) - \tilde{\rho}^1(\mathbf{r}),$$

where $\tilde{\rho}(\mathbf{r})$ is the soft auxiliary charge density which can be calculated from the auxiliary wave function

$$\tilde{\rho}(\mathbf{r}) = \sum_n f_n \langle \tilde{\psi}_n | \mathbf{r} \rangle \langle \mathbf{r} | \tilde{\psi}_n \rangle,$$

and on-site charge densities are defined as

$$\rho^1(\mathbf{r}) = \sum_{ij} \rho_{ij} \langle \phi_i | \mathbf{r} \rangle \langle \mathbf{r} | \phi_j \rangle, \quad \widetilde{\rho}^1(\mathbf{r}) = \sum_{ij} \rho_{ij} \langle \widetilde{\phi}_i | \mathbf{r} \rangle \langle \mathbf{r} | \widetilde{\phi}_j \rangle$$

The occupancy ρ_{ij} can be found from auxiliary wave function applying the projector function,

$$\rho_{ij} = \sum_n f_n \langle \widetilde{\psi}_n | \widetilde{p}_i \rangle \langle \widetilde{p}_j | \widetilde{\psi}_n \rangle$$

2.7 Comments

In the work that follows we shall base our calculations on the density functional theory. We shall solve the KS equation in a projector augmented plane wave basis. The molecular dynamics can be carried out using the Hellman-Feynman forces. These are all embodied in the Vienna ab-initio simulation package (VASP). This simulation package will be our main tool in the work presented in this thesis. This chapter represents an understanding of the theoretical basis of the simulation package.

Chapter 3

Electronic and geometric properties of pristine ZnO clusters

In this chapter we study small stoichiometric clusters of $(\text{ZnO})_n$ in the size range $2 \leq n \leq 12$ ¹. We shall present ground state geometries, binding energies, relative stabilities and HOMO-LUMO gaps of these clusters. We shall discuss how these properties evolve with the increasing size of clusters.

3.1 Introduction

Nano-structures of ZnO have emerged as promising materials because of their prospects in applications in catalytic [20], electrical [21], opto-electronic [22] and quantum devices [23]. The understanding of structural and electronic properties is important for better optimization of these materials to enhance their applicability. We have attempted to study these properties by performing the first principles calculations on small clusters of ZnO. As clusters bridge the space between the small molecule, the nano-particle and

¹This Chapter is based on the papers:

(i) *Band-gap variation in Mg- and Cd-doped ZnO nanostructures and molecular clusters*, Phys. Rev. B 76 (2007) 195450; **Manoj K Yadav**, Manoranjan Ghosh, Ranjit Biswas, Arup K Raychaudhuri, Abhijit Mookerjee and Soumendu Datta.

(ii) *Study of the electronic and structural properties of ZnO clusters*, Int. J. Mod. Phys. B (in press); **Manoj K Yadav**, Biplab Sanyal and Abhijit Mookerjee.

bulk materials, their study will be helpful for better understanding the evolution of various properties with the increase in size of the clusters. Moreover, clusters display many unique properties due to their specific geometry and quantum confinement effect. While there are hosts of studies on elemental clusters, very few reports on bi-elemental semiconductor clusters can be found [24, 25, 26]. First principles studies on small clusters of ZnO have been carried out earlier by Matxain *et al.* [24]. Bulgakov *et al.* [27] produced small ZnO clusters by laser ablation method and investigated them using time of flight mass spectrometry.

It will be useful to carry out a systematic first-principles theoretical study of clusters of $(\text{ZnO})_n$ using the soft-pseudo-potential technique ideally set up for clusters containing an element with d -electrons whose potentials are pretty localized and deep. Such a formulation is ideal for Zn containing clusters. This chapter aims toward this goal. We shall determine the geometrical structures of ground states as well as that of the next higher energy isomers of the clusters in the size range $2 \leq n \leq 12$. We shall examine the binding energy and the HOMO-LUMO gaps of the clusters as a function of their size. These parameters will be helpful in determining relative stability of clusters. The studies in this chapter lay the foundation of Chapter 4 where we shall focus on variation of band gap in Mg/Cd doped ZnO nanostructures and molecular clusters.

3.2 Methodology

Our electronic and total energy calculations and shape optimization of the clusters will be based on the projector augmented wave method (PAW). Blöchl [18] combined the density functional based multiple scattering (the linearized augmented plane wave LAPW) and the pseudo-potential (PP) approaches to present the computationally elegant, transferable and accurate PAW. Kressé and Joubert [19] modified and codified this PAW technique into the Vienna ab-initio pseudo-potential package (VASP) on which our present work

will be based.

The mathematics of the PAW method has been described in detail elsewhere [18]. We shall comment on the following :

- The electron-ion interaction were described by the pseudo-potential based ideas. This is implicit in the PAW methodology.
- We have used the exchange-correlation functional suggested by Perdew, Burke and Ernzerhof [12].
- The shape optimization was carried out via conjugate gradient algorithm implemented in VASP.
- The starting point of shape optimizations were educated guesses and, for the smaller clusters, these guesses were based on the results of Matxain *et.al.* [24]. The cluster was then relaxed until the energy was minimized and the local forces were smaller than 0.01 eV/Å.

The binding energies of $(\text{ZnO})_n$ clusters are defined as follows :

$$E_B = E[n] - n E[\text{Zn}] - n E[\text{O}] \quad (3.1)$$

where $E[n]$ is the total energy of the $(\text{ZnO})_n$ cluster, $E[\text{Zn}]$ is the energy of a single Zn atom and $E[\text{O}]$ is the energy of a single O atom.

The second difference in binding energy can be calculated as

$$\Delta_2 E(n) = 2 E(n) - E(n+1) - E(n-1), \quad (3.2)$$

where $E(n+1)$ and $E(n-1)$ are energies of $(\text{ZnO})_{n+1}$ and $(\text{ZnO})_{n-1}$ clusters respectively. The quantity $\Delta_2 E(n)$ represents the relative stability of a cluster of size n with respect to its neighbors.

3.3 Results and Discussion

We shall begin with a brief description of the ground state and next higher energy local minimum state structures of $(\text{ZnO})_n$ clusters, before we describe overall trends with size.

The structures of the ground and higher energy local minimum states of $(\text{ZnO})_n$ clusters for $n = 2$ to 7 are shown in Fig. 3.1. The ground state of $(\text{ZnO})_2$ is a rhombus with the Zn and O atoms in a trans configuration. The Zn-O distances are 1.902 Å and O-Zn-O and Zn-O-Zn angles 104.67° and 75° respectively. The structure has a point group symmetry D_{2h} . The local minimum state is a trapezium with Zn and O atoms in a cis configuration. The Zn-O distances at 1.976 Å are considerably larger than the ground state structure.

The ground and next higher energy local minimum state structures of $(\text{ZnO})_3$ are both planar. The ground state belongs to D_{3h} symmetry with a triangle of Zn atoms connected by O atoms. The three Zn atoms form an equilateral triangle. The Zn-O distance has now diminished to 1.832 Å : less than that in $(\text{ZnO})_2$. As expected, the binding energy of the trimer is more than that of the dimer. The Zn-O-Zn angles are 91° and O-Zn-O angles 149.4° . The local minimum state is a complex structure belonging to the C_s symmetry. The ground state of $(\text{MgO})_3$ has very similar structure. However Calvo [25] finds this to be regular hexagon, whereas we find a distorted hexagon with different O-Zn-O and Zn-O-Zn angles.

We continue to get planar ring-like structures for $n=4$ also. This is a distorted square with Zn-O-Zn angle 100.7° and O-Zn-O angle of 170° . It belongs to the D_{4h} symmetry. We note that as the cluster size increases, the O-Zn-O angles tend towards linearity from $\sim 105^\circ$ for $(\text{ZnO})_2$ to 149° in $(\text{ZnO})_3$ to 170° here. The next higher local minimum state, for the first time, is a distorted three-dimensional cube with two distorted squares with O-Zn-O angles of 98.4° and Zn-O-Zn angles of 81° . This structure belongs to the T_d symmetry. The ground state structure of $(\text{MgO})_4$ was found by Calvo [25] as a perfect

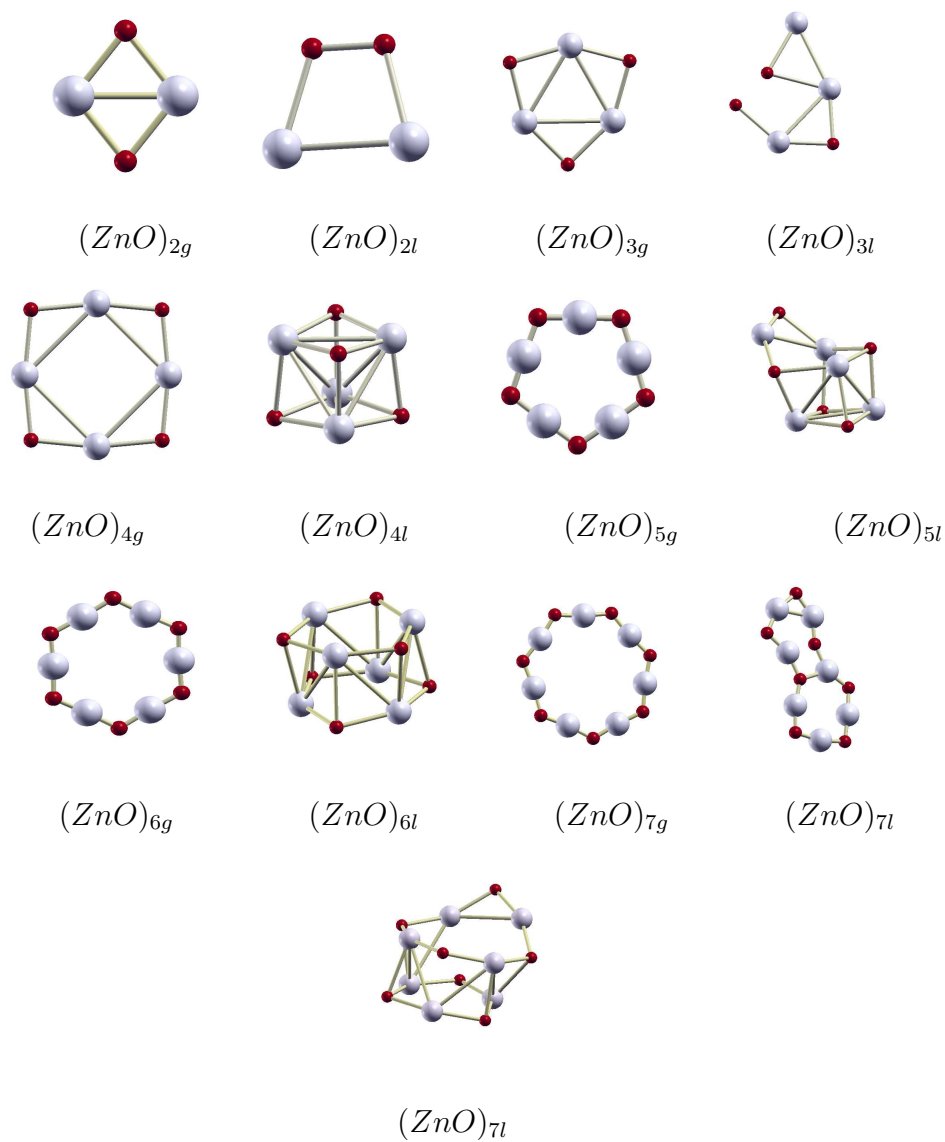


Figure 3.1: $(ZnO)_n$ clusters for $n=2$ to 7; large light spheres represent Zn atoms and smaller darker (red) spheres the O atoms. The subscripts g and l stand for global and local minima structures respectively.

cube. This is in contrast with ZnO. However, Calvo used an empirical potential based molecular dynamics. It would be interesting to repeat those calculations from a first-principles approach like ours.

As the cluster size increases, for $(\text{ZnO})_5$ we carry on getting the planar ring-like structures as the ground state. The ground state structure of $(\text{ZnO})_5$ belongs to the symmetry D_{5h} with Zn-O-Zn angles of 110° and O-Zn-O angles almost linear at 178° . The ring begins to deviate slightly from planarity with the O atoms falling slightly below the Zn plane. The local minimum structure is again three dimensional with a distorted square $(\text{ZnO})_2$ unit and a distorted hexagonal $(\text{ZnO})_3$ unit. Again, the ground state of $(\text{MgO})_2$, as reported by Calvo [25], is very different : made out of a $(\text{MgO})_4$ unit and a $(\text{MgO})_2$ unit.

The ground state for $(\text{ZnO})_6$ continues to be an almost planar ring with D_{6h} symmetry. The Zn-O-Zn angles are 116° and the O-Zn-O angles are almost linear at 179.7° . The next higher energy structure is the three dimensional structure with two $(\text{ZnO})_3$ units belonging to the D_{3d} symmetry sitting one above another. For $(\text{ZnS})_6$ this is the ground state, while $(\text{MgO})_6$ has a prism like ground state. At this stage, we begin to notice the differences between ZnO and MgO which have very different structures in the bulk and these structures in the clusters give some inklings of the bulk ones.

The ground state for $(\text{ZnO})_7$ is again a planar ring belonging to D_{7h} symmetry. The Zn-O-Zn angles are 122° and O-Zn-O angles are linear. We have observed that there is a competition between planar and three-dimensional structures. For the smaller clusters planar structures, and in particular, ring-like planar structures are more stable. At $(\text{ZnO})_7$ one more planar structure with a $(\text{ZnO})_4$ ring connected with a $(\text{ZnO})_3$ ring becomes the next higher energy local minimum state. However, there is also a three dimensional structure which is a capped version of the $(\text{ZnO})_6$ three-dimensional structure, and is very near in energy to the planar one.

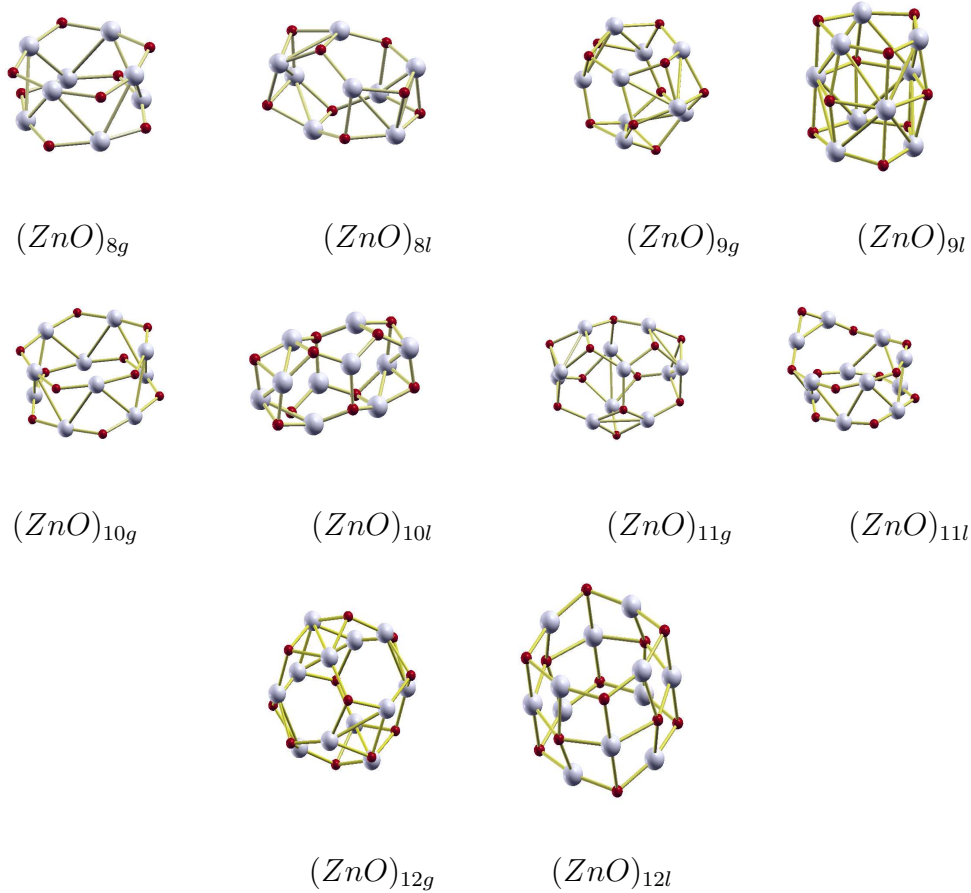


Figure 3.2: $(\text{ZnO})_n$ clusters for $n = 8$ to 12 ; large spheres represent Zn atoms and smaller spheres the O atoms. The subscripts g and l stand for global and local minima structures respectively.

Figure 3.2 shows the ground state and next higher energy structures for $(\text{ZnO})_n$; $n=8 \dots 12$. When we come to the critical size of $(\text{ZnO})_8$ there is a transition of stability from planar rings to three-dimensional ground state structures. By the time we reach $(\text{ZnO})_7$ the difference in energy between the planar and the three-dimensional structures is already less than 0.5 eV [see Fig. 3.6 (Right)]. For $(\text{ZnO})_8$ the ground state structure which is two $(\text{ZnO})_4$ rings attached atop each other with $(\text{ZnO})_2$ units, belongs to D_{4d} symmetry. The next higher energy isomer is also three dimensional and made up out of four $(\text{ZnO})_3$ and six $(\text{ZnO})_2$ rings. It is at this size that formation of spheroidal structures

reminiscent of fullerenes reported by Behrman *et al.* [28] begins to show up. Up to size $(\text{ZnO})_7$ the Zn-O bond lengths kept decreasing in the planar ring structures. Now, as the three-dimensional structures stabilize the average Zn-O bond length suddenly increases to 1.859 Å. The Zn-O-Zn angles are now 112° and O-Zn-O angles 158° . It should be noted that none of the constituent rings of the three-dimensional structures are truly planar. The Zn atoms sit on a plane, but the O atoms deviate alternately from it.

The ground state structures for clusters with $n \geq 9$ are built out of $(\text{ZnO})_3$ and $(\text{ZnO})_2$ units, i.e hexagons and rhombus. This tendency of forming spheroidal structures with these units is characteristic of ZnO clusters with large n . The $(\text{ZnO})_{12}$ is the most spheroidal in shape in the size range $2 \leq n \leq 12$. In this it resembles C_{60} , but unlike it, it is unstable with respect to the macroscopic crystal. These structures differ from the fullerenes in the sense that while fullerenes have pentagons and hexagons, these structures have rhombus and hexagons. Here we do not expect pentagons, since that will force like atoms to bond, which is energetically unfavorable in the case of ZnO. This tendency of forming spheroidal structures appear to be rather surprising that atoms interacting via central forces spontaneously form hollow spheroidal shapes with all the atoms on the surface. We would have expected compact shapes as found by Behrman *et al.* [28] for NaCl. As the size increases, the Zn-O distance decreases towards the bulk value. The higher energy isomers for $n = 9, 10, 11$ and 12 are more open structures reminiscent of MgO ground states found by Calvo [25]. For ZnO these are not stable shapes.

Figure 3.3 shows the average Zn-O distance as a function of cluster size. The figure indicates an initial decrease in the average Zn-O distance as we go up the planar ring structures indicating stronger Zn-O bonding. This stronger bonding leads to less than linear O-Zn-O shapes at the smaller rings to almost linear O-Zn-O shapes at $n=7$. At $n=8$ there is a sharp change which is a signature of the transition to stable three dimensional shapes. The ground state remains three-dimensional as cluster size increases. The Zn-O bond length decreases again with further increase in size. The stability of these

Table 3.1: The table shows a summary of the energetics and bond lengths for $(\text{ZnO})_n$ clusters with $n=2, \dots, 12$.

Size n	E_B (eV)	E_B/ZnO (eV)	E_g (eV)	$\Delta_2 E$ (eV)	$d_{\text{Zn-O}}$ (avg) Å
1	2.12	2.12	0.34		1.70
2	8.16	4.08	1.08	-1.83	1.90
3	16.04	5.35	2.76	0.82	1.83
4	23.12	5.78	2.85	0.63	1.80
5	29.54	5.91	2.93	0.27	1.78
6	35.70	5.95	2.81	0.13	1.78
7	41.74	5.96	2.90	-0.31	1.77
8	48.08	6.01	1.97	-0.18	1.99
9	54.60	6.07	1.97	0.15	1.96
10	60.97	6.10	2.34	-0.76	1.99
11	68.10	6.19	1.95	-0.66	1.95
12	75.89	6.32	2.33		1.94

three dimensional structures is driven from the increased coordination whereas for ring structures the highly obtuse O-Zn-O angle is mainly responsible for their stability. In an earlier paper by Finocchi and Noguera [29] on Li_xO_y , it has been proposed that mean coordination number may also provide insight into the planar to three-dimensional transition. However, for Li_xO_y , the number of constituent atoms can vary causing gradual increase in average coordination number. For $(\text{ZnO})_n$ the number of Zn and O atoms are equal for every cluster and the coordination number is either 2 for $n \leq 7$ and 3 for $n > 7$. Thus, the transition at $n=8$ agrees with the proposition of Finocchi and Noguera [29].

We next examine the energetics of the clusters. This is summarized in Table 3.1. Figure 3.4 (Left) shows the binding energy in $(\text{ZnO})_n$ clusters per ZnO unit. The filled circles indicate the calculated energies in eV and the line shows the fitted form. The fitted

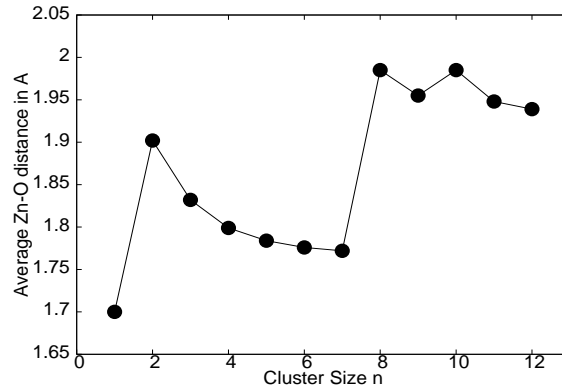


Figure 3.3: The average Zn-O distance as a function of size of clusters.

expression is given by

$$E_b = -24.33 + 45.12 n^{\frac{1}{3}} - 22.53 n^{\frac{2}{3}} - 3.78 n \quad (3.3)$$

The form is empirical and has been suggested by many authors [24, 25]. It is useful in predicting the binding energy of larger clusters. The binding energy per ZnO unit in bulk ZnO is around 7.52 eV [30]. The binding energy curve tends towards this value slowly but we are nowhere near approaching this limit for clusters as small as 12 units.

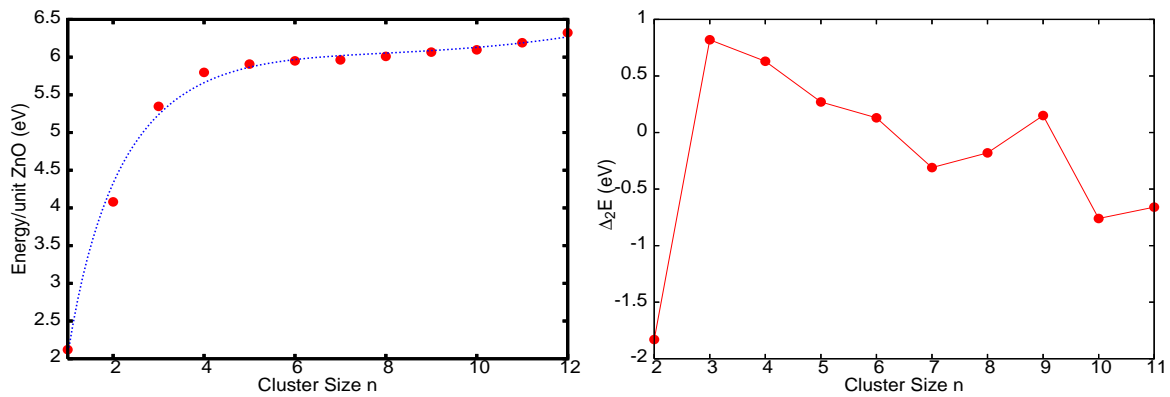


Figure 3.4: (Left) Binding energy per ZnO unit versus size of cluster n . The circles are results of this work, while the dotted line represents the fitted function (3.3). (Right) Second difference in binding energy versus size of clusters n .

The plot of second difference in binding-energies $\Delta_2 E$ (calculated using Eqn. 3.2) as a function of size of clusters is shown in Fig. 3.4 (Right). The second difference in

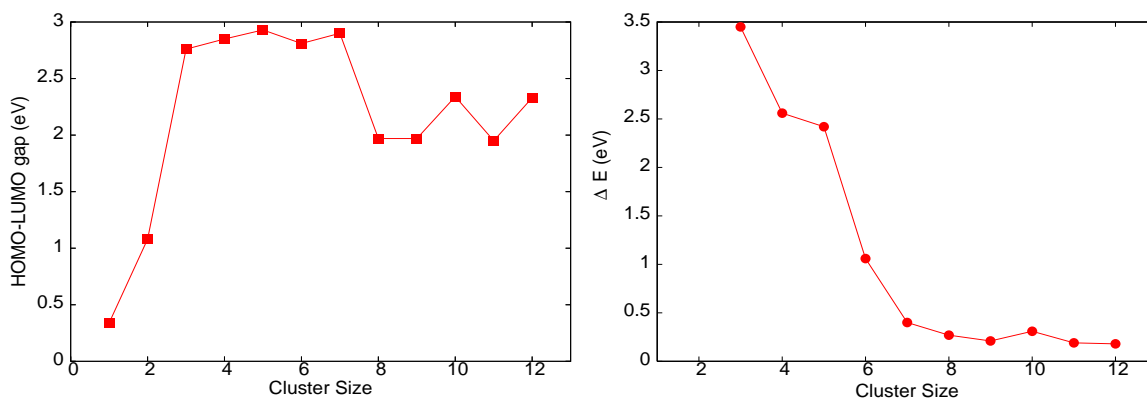


Figure 3.5: (Left) HOMO-LUMO gap versus size of clusters n . (Right) Energy difference between ground states and the corresponding next higher energy isomers.

binding energy of a particular cluster indicates its relative stability with respect to its neighbouring sizes. The peaks in the second difference in binding energy indicate higher relative stability of the corresponding cluster, and can be compared with peaks in mass-spectrograph of ZnO clusters. These stable clusters then neither add another unit and stabilize themselves nor shed a unit to do so. Bulgakov [27] have carried out laser ablation synthesis of ZnO clusters and have shown from a time of flight mass spectra the stability of clusters of sizes $n=6$, 9 and 11. Their proposed shapes for the $n=9$ and $n=11$ clusters closely agree with our prediction.

The stability of a particular structure can also be predicted with the magnitude of HOMO-LUMO gap, E_g . A large HOMO-LUMO gap implies low chemical reactivity because it is energetically less favourable to add electrons to a high-lying LUMO or extract electrons from a low-lying HOMO, and thereby prohibiting the formation of a larger cluster or breakup into smaller ones [31]. Thus the structure having larger HOMO-LUMO gap is more stable and vice versa. Figure 3.5 (Left) shows the HOMO-LUMO gaps as a function of cluster size. As expected large gaps in the planar ring structures indicate their greater stability. There is a transition at $n=8$, as expected, a signature of the planar to three-dimensional structures. The odd even oscillation of HOMO-LUMO gap usually seen in elemental clusters [32, 33] is not evident here.

Finally we show in Fig. 3.5 (Right), the energy difference between the ground states and the corresponding next higher energy isomers as a function of cluster size. The figure clearly shows that this energy difference is small for the larger clusters, which then tend to isomerize at higher temperatures. Also, there is a sharp drop around $n=8$. This indicates that the lower sized planar ring-structures are particularly stable and difficult to isomerize. This is consistent with our other analysis.

3.4 Summary and Remarks

We have carried out a first-principles study of the structural and energetic characteristics of $(\text{ZnO})_n$ clusters in the size range $2 \leq n \leq 12$. Our analysis shows that up to $n=7$ planar ring structures are stable. However, at $n=8$ there is a transition to three-dimensional stable structures. This transition is indicated by the sharp changes in HOMO-LUMO gap, average bond length and also by the change in coordination from 2 to 3. The larger $(\text{ZnO})_n$ clusters are roughly spheroidal and made up of $(\text{ZnO})_2$ and $(\text{ZnO})_3$ units. The stable structures around $n=11$ and 12 resembles fullerenes and this has led several authors to speculate whether ZnO clusters form a “new class” of fullerenes. The analysis of the binding energies, second derivatives of the binding energies and the HOMO-LUMO gaps clearly indicate stability of $n=3, 4, 6, 9$ and 11 sized clusters. This is in qualitative agreement both with earlier theories and time of flight mass spectrographic experiments.

3.5 Comments

The study of pristine ZnO clusters was a prelude to the study of doped ZnO. The idea would now be to see how Mg/Cd doping affects the electronic properties of ZnO clusters. This will be presented in the following chapters.

Chapter 4

Tailoring the band gap of ZnO by doping

This chapter deals with the defect induced variation of band gap of ZnO¹. Two types of substitutional defect, *viz.* Mg and Cd have been considered. The study extends over two size regimes: nanostructures and molecular clusters of ZnO. We aim to investigate the trend of variation of energy gap in both nanostructures and clusters of ZnO when these are doped with Mg and Cd.

4.1 Introduction

ZnO is a direct band gap semiconductor with large band gap (3.37 eV) and large exciton binding energy (59 meV). The band gap of direct nature is useful for efficiency of optical devices and large band gap is useful for short wavelength emissions. The large exciton binding energy is suitable for high temperature operations. Apart from these useful properties ZnO is cheaper, abundant and its single crystal can be synthesized easily. All these properties make ZnO an important material for applications in optoelectronic [34, 35, 36] and quantum devices [23, 37]. A large variety of ZnO nano-structures like nano-particles, nano-rods, nano-tubes and nano-wires, have been synthesized [38, 39] and they have been successfully used in, for example, optical devices [40, 41].

¹This chapter is based on the paper: *Band-gap variation in Mg- and Cd-doped ZnO nanostructures and molecular clusters*, Phys. Rev. B **76**, 195450 (2007); **Manoj K Yadav**, Manoranjan Ghosh, Ranjit Biswas, Arup K Raychaudhuri, Abhijit Mookerjee and Soumendu Datta.

Tailoring band gap of a material plays an important role in making the material suitable for application to various devices operating at different frequencies. There are various techniques for engineering band gap of a system. Shan *et al.* [42] have reported pressure induced variation of band gap of Al doped GaN. In the nano size regime the band gap of a system can be tuned by playing with the dimension of the system [43]. Another way of tailoring band gap of a material is by doping the material with suitable dopants. In this method one can either increase or decrease the band gap of a material by doping it with suitable dopants. Banking on this method there are several reports [44, 45, 46, 47, 48] showing the variation of band gap of ZnO by doping it with Mg or Cd. Ohtomo *et al.* [44] alloyed ZnO with MgO using the pulsed laser deposition (PLD) method, and reported increase in band gap in the alloy. Decrease in band gap in Cd doped ZnO has been reported by several authors [46, 47, 48]. Makino *et al.* [47] have studied alloying of ZnO with CdO using PLD method, and found decrease in the band gap in the alloy. Wang *et al.* [46] investigated the effect of Cd substitution in $Zn_{1-x}Cd_xO$ nano-rods and nano-needles. They also found decrease in the band gap with increasing concentration of Cd. Recently Wang *et al.* [49] reported a band gap of 3.66 eV in Mg doped ZnO nanocrystals at 15% of Mg concentration. In the case of Cd doped ZnO they could achieve a band gap as low as 2.9 eV at 10% of Cd concentration.

While there are host of experimental works showing the variation of band gap of doped ZnO, there are very few theoretical works in this direction [50, 51]. We have carried out first principles calculation on the variation of HOMO-LUMO gap in Mg/Cd doped small ZnO clusters. As clusters bridge the gap between a molecule and the bulk material, in this work we have tried to understand our experimental findings on $Zn_{1-x}(Mg,Cd)_xO$ nanostructures (10-15 nm) through a first principles theoretical study of clusters of sizes about 6 Å. Though it may not be fair to compare two systems which differ in size by an order in magnitude, the aim of this investigation is to look at qualitative trend with varying doping concentration.

With our findings from Chapter 3, we have chosen highly symmetrical cage-like stable clusters $(\text{ZnO})_9$ and $(\text{ZnO})_{12}$ for Mg/Cd doping. The “band gap” which arises out of the Kohn-Sham *virtual* orbital based density of states are always underestimated. We shall therefore concentrate on the *change* in the band gap (or the HOMO-LUMO gap for finite system) on doping, with the expectation that the errors in the doped and undoped cases compensate each other.

For the synthesis of $\text{Zn}_{1-x}(\text{Mg,Cd})_x\text{O}$ alloy nano-structures we have chosen a solution growth method for clear understanding of lower doping efficiency of Cd than that of Mg. In this method mixing occurs at atomic level, so the material made by this method is close to thermodynamic equilibrium phase. Therefore the doping efficiency of Mg and Cd into ZnO can be explained on the basis of cohesive binding energy of the corresponding alloys. The change in the binding energies of $\text{Zn}_{1-x}\text{Mg}_x\text{O}$ and $\text{Zn}_{1-x}\text{Cd}_x\text{O}$ alloy molecules from the parent compound ZnO determines the doping efficiency of corresponding dopant atoms.

One needs to be cautious while investigating the effect of doping on the band gap of ZnO nano-structures because in the quantum confinement regime band gap becomes function of size [52]. In our experimental work we have used nano-structures of size 10-15 nm which lies beyond the quantum confinement limit ($\leq 5\text{nm}$). In the size regime we are working (10-15 nm), the variation in band gap for small fluctuations in size ($\sim 5\text{ nm}$) is very small (0.06 eV) compared to the change in band gap observed as the effect of doping.

4.2 Experimental Study

Before we describe our theoretical work on doping of ZnO clusters with Mg and Cd, we shall first describe an experimental study on doped ZnO nano-structures. The experiment was carried out in collaboration with experimental group of A.K. Raychaudhuri. We should be pertinent to note that the experiments were done on nano-structures of size 10-

15 nm. Given our computational resources, first principles studies on such large clusters was not possible. So our idea would be to look at trends both with increasing size and doping concentration.

4.2.1 Synthesis

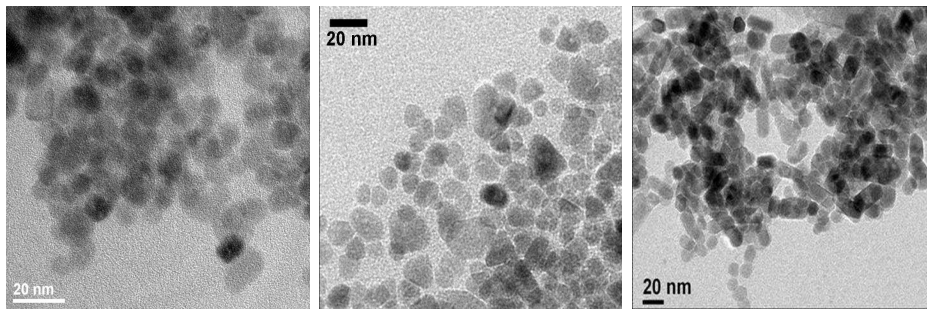


Figure 4.1: TEM images of (Left) undoped ZnO nano-structures, (Middle) Mg doped ZnO nano-structures and (Right) Cd doped ZnO nano-structures.

ZnO nano-structures were synthesized using acetate route. A 0.03 M NaOH solution in ethanol was added in 0.01 M solution of $\text{Zn}(\text{CH}_3\text{COOH})_2 \cdot 2\text{H}_2\text{O}$ in ethanol kept at 65°C . The final solution was stirred and heated at 65°C for two hours. This method allows precipitation of ZnO nano-particles and avoids precipitation of hydroxides if the temperature is above 60°C . For the purpose of making $\text{Zn}_{1-x}\text{Mg}_x\text{O}$ alloys, we added different amounts of $\text{Mg}(\text{CH}_3\text{COOH})_2 \cdot 4\text{H}_2\text{O}$ to the $\text{Zn}(\text{CH}_3\text{COOH})_2 \cdot 2\text{H}_2\text{O}$ solution for different doping concentration. The dispersions containing $\text{Zn}_{1-x}\text{Mg}_x\text{O}$ nano-particles were washed with water by centrifugation. Finally the precipitates were collected by dispersing them in ethanol for optical measurements.

The fabrication of $\text{Zn}_{1-x}\text{Cd}_x\text{O}$ nano-structures was not possible under similar conditions as described above. This is because of the fact that incorporation of Cd into ZnO leads to the decrease in cohesive binding energy. To achieve proper alloying, the $\text{Zn}_{1-x}\text{Cd}_x\text{O}$ nano-structures were synthesized under high pressure to obtain higher boil-

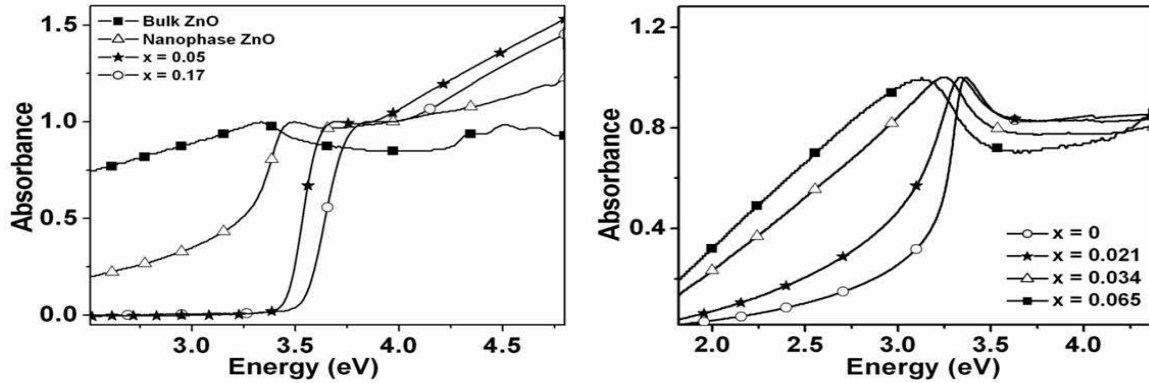


Figure 4.2: Absorption spectra of the nano-structures: (Left) Mg-doped nano-structure and (Right) Cd-doped nano-structure.

ing point of ethanol (230°C). In order to synthesize $\text{Zn}_{1-x}\text{Cd}_x\text{O}$ alloy nano-structures, a clear solution of $0.015\text{ M Zn}(\text{CH}_3\text{COOH})_2 \cdot 2\text{H}_2\text{O}$, 0.045 M NaOH and controlled amount of $\text{Cd}(\text{CH}_3\text{COOH})_2 \cdot 2\text{H}_2\text{O}$ was prepared. Then the solution was taken in a Teflon lined autoclaves preset at 230°C . The $\text{Zn}_{1-x}\text{Cd}_x\text{O}$ nano-structures thus prepared after two hours of reaction within the autoclaves, were centrifuged and washed by water. The precipitates were collected by dispersing in ethanol for optical measurements.

4.2.2 Characterization

The amounts of incorporated dopant atoms in the alloy nano-structures were found by inductively coupled plasma atomic emission spectroscopy (ICP-AES). The maximum incorporation achieved in $\text{Zn}_{1-x}\text{Mg}_x\text{O}$ and $\text{Zn}_{1-x}\text{Cd}_x\text{O}$ were $x=0.17$ and 0.065 for the two alloys respectively. Incorporation beyond these values could not be achieved as the phase segregation starts to take place. The average size of the nano-structures were determined by transmission electron microscope (TEM) as well as X-ray diffractometer (XRD) data. The average size of undoped ZnO nano-structures lies in the range $10\text{-}15\text{ nm}$ as seen by TEM image shown in the left panel of Fig. 4.1. The size of the alloy nano-structures were also found to lie in the same range. Two representative TEM images of $\text{Zn}_{1-x}\text{Cd}_x\text{O}$ and

$\text{Zn}_{1-x}\text{Mg}_x\text{O}$ alloy nano-structures are shown respectively in the middle and right panels of Fig. 4.1. The sizes of the nano-structures were also determined by Williamson Hall analysis of the XRD data and the results agree well with the TEM results.

4.2.3 Results and Analysis

The direct band gap values of ZnO and its alloy nano-structures have been determined by monitoring the fundamental absorption edges of the room temperature absorption spectra shown in Fig. 4.2. In the left panel of that figure we can see the gradual blue shift of the fundamental absorption edge with the increase of Mg concentration. Also the excitonic peak appearing in the absorption spectra of ZnO persists even after considerable increase in Mg incorporation. The band gap of $\text{Zn}_{1-x}\text{Mg}_x\text{O}$ nano-structures increases monotonously as we increase the Mg concentration. At 16.8% Mg concentration we could achieve a band gap of 3.99 eV which is equivalent to 12.39% enhancement. On the other hand Cd doped nano-structures show gradual red shift in fundamental absorption edge as shown in the right panel of Fig. 4.2. We could achieve a band gap as low as 2.87 eV at only 6.50% Cd concentration. Kukreja *et al.* [48] have reported 12.76% enhancement in the band gap in Mg-doped ZnO alloy at 14% Mg concentration. In the case of Cd-doped ZnO alloy they have found about 13.95% decrease in the band gap at 8.0% Cd concentration. In both cases our results compare well even though the method of fabrications were quite different. We have fabricated nano-structures via solution route whereas Kukreja *et al.* [48] have made alloy by the PLD method. Interestingly for the $\text{Zn}_{1-x}\text{Cd}_x\text{O}$ alloy nano-structures, the excitonic behavior of the absorption spectra diminishes quickly as soon as Cd incorporation starts to take place. Thus the large excitonic binding energy of ZnO (60 meV) decreases sharply for $\text{Zn}_{1-x}\text{Cd}_x\text{O}$ contrary to the case of $\text{Zn}_{1-x}\text{Mg}_x\text{O}$.

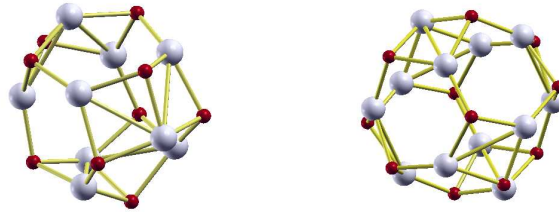


Figure 4.3: Ground state structures of (Left) $(\text{ZnO})_9$ and (Right) $(\text{ZnO})_{12}$ clusters. Large light (grey) spheres represent Zn atoms and smaller dark (red) spheres the O atoms.

4.2.4 Doped ZnO clusters

The computational details for study on clusters are similar to those outlined in Chapter 3. Figure 4.3 shows ground state structures of pristine $(\text{ZnO})_9$ and $(\text{ZnO})_{12}$ clusters. These are almost spherical in shape and are made up of units of rhombus and hexagons. The analysis of second difference in binding energy and HOMO-LUMO gap in Chapter 3 showed that these structures are relatively more stable, and therefore we have chosen them for Mg/Cd doping. We have carried out substitutional doping of these clusters, replacing Zn atom(s) by dopant atom(s). We have tried to place the dopant atoms as random as possible to avoid practically unimportant segregated structures. The optimized structures of $(\text{ZnO})_{12}$ cluster doped with 5 dopant atoms are shown in Fig. 4.4. The structures doped with fewer atoms of Mg and Cd are not shown. The formation energy for doping X (Mg,Cd) at Zn site of $(\text{ZnO})_{12}$ can be calculated using the relation,

$$E_f = E[\text{Zn}_{11}\text{XO}_{12}] - E[\text{Zn}_{12}\text{O}_{12}] - \mu_X + \mu_{\text{Zn}}, \quad (4.1)$$

where $E[\text{Zn}_{11}\text{XO}_{12}]$ and $E[\text{Zn}_{12}\text{O}_{12}]$ are energies with and without doping. μ_X and μ_{Zn} are chemical potentials for X and Zn respectively. The formation energies for Mg and Cd doping are found to be -2.516 and 1.157 eV respectively, which indicate that such dopings are reasonably achievable.

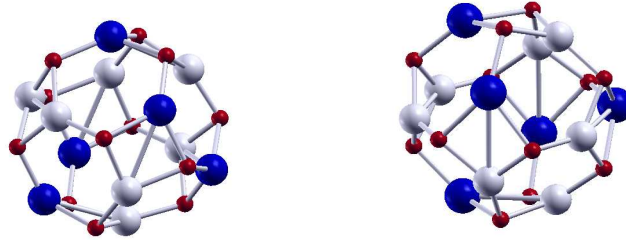


Figure 4.4: Structures of (Left) Mg-doped $(\text{ZnO})_{12}$ cluster and (Right) Cd-doped $(\text{ZnO})_{12}$ cluster. Large light (grey) spheres represent Zn atoms and smaller darker (red) spheres the O atoms. The dopant atoms (Mg or Cd) are shown as large darker (blue) spheres.

The left panel in Fig. 4.5 shows the variation of binding energy of the clusters with increasing concentration of dopant atoms. The total binding energy of these doped clusters increases with increasing concentration of Mg whereas it decreases with increasing Cd concentration. This means that doping with Mg increases the stability of the clusters whereas doping with Cd decreases stability. This is an important observation that connects with the following experimental facts : (i) low doping efficiency of Cd compared to Mg and (ii) increase in photo-luminescence peak of $\text{Zn}_{1-x}\text{Cd}_x\text{O}$. The lower stability of $\text{Zn}_{1-x}\text{Cd}_x\text{O}$ clusters give rise to fluctuations in the Cd content of the material as well as overall lower Cd incorporation into ZnO as observed by several authors [47, 53]. The larger value of formation energy for Cd doping than that for Mg doping also reflects that Cd incorporation is less favorable compared to Mg incorporation.

The middle panel of Fig. 4.5 shows the variation of HOMO-LUMO gap with change in dopant concentration in $(\text{ZnO})_9$ and $(\text{ZnO})_{12}$ clusters. In both clusters the HOMO-LUMO gap increases with increase in Mg concentration while it decreases with increase in Cd concentration. A cluster with a larger HOMO-LUMO gap is more stable and vice-versa. Therefore the fact that increase in Mg concentration increases the HOMO-LUMO

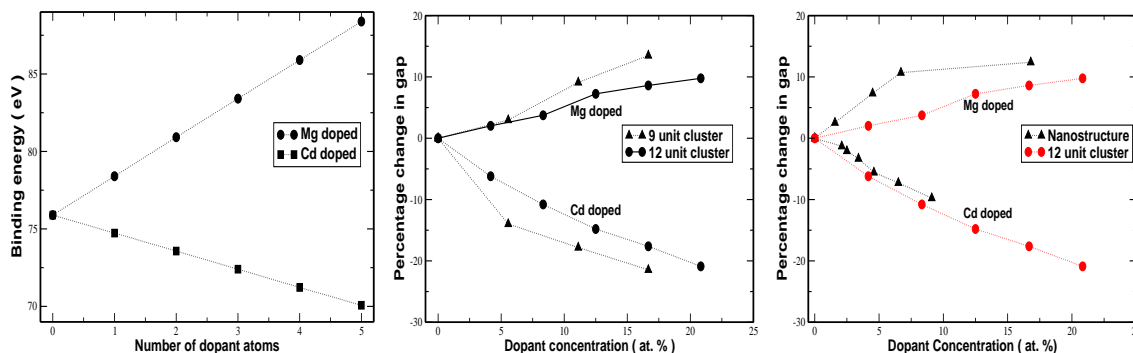


Figure 4.5: (Left) Variation of the binding energy with Mg and Cd doping. (Middle) Variation in energy gaps with doping for $(\text{ZnO})_n$ clusters for $n=9$ and 12. (Right) Comparison of theoretically obtained energy gaps in doped $(\text{ZnO})_{12}$ cluster with experimental energy gaps in doped nanostructures. The dotted lines are for convenience of visualization.

gap and increase in Cd Concentration decreases HOMO-LUMO gap is consistent with stability character shown by binding energy result. We also notice that as the size of the clusters increases (from $n=9$ to $n=12$) the change in the band-gap decreases [Fig. 4.5 (middle)].

The experimental variation in band gap in nano-structure and the theoretically obtained HOMO-LUMO gap in $(\text{ZnO})_{12}$ clusters with increasing concentration of Mg and Cd are compared in the right panel of Fig. 4.5. Though it is not fair to compare the variation in HOMO-LUMO of doped $(\text{ZnO})_{12}$ clusters with the band gap of rather larger nano-structures, it is interesting to note that the trend is qualitatively similar. This reinforces our belief that if we carry out theoretical investigations on much larger clusters, which is computationally very expensive, we will still get the same qualitative trends as seen here.

Can we try to understand why the HOMO-LUMO gap increases when ZnO clusters are doped with Mg and decreases when doped with Cd? To answer this question, let us look at the cluster $(\text{ZnO})_{12}$ and the two clusters $\text{Mg}_5\text{Zn}_7\text{O}_{12}$ and $\text{Cd}_5\text{Zn}_7\text{O}_{12}$ as shown in Fig. 4.4. All the three clusters are constructed out of six-membered and four-membered

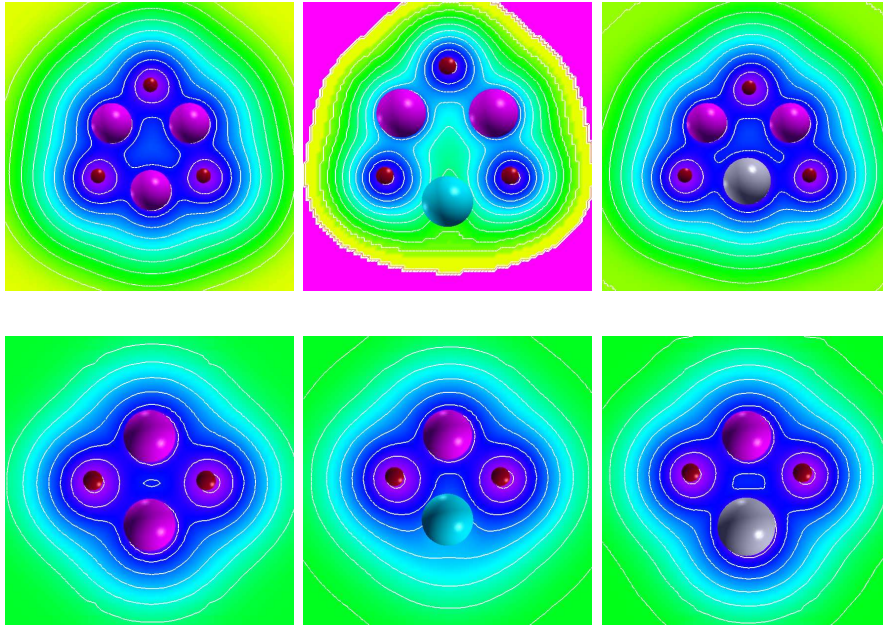


Figure 4.6: Charge densities (Left) pristine ZnO, (Middle) Mg doped ZnO, and (Right) Cd doped ZnO for (Top) $(\text{ZnO})_3$ ring and (Bottom) $(\text{ZnO})_2$ ring.

rings. Let us look at the charge densities on planes through one of these rings. These are shown in Fig. 4.6. The figure shows the Zn^{2+} , Mg^{2+} and Cd^{2+} ions sitting in the sea of valence electron cloud. As compared to the pristine ZnO cluster, wherever a Mg^{2+} ion sits, the charge density is pushed away from it towards the Zn^{2+} ions. The reverse is true wherever a Cd^{2+} ion sits.

The consequence of this is that in the Mg doped ZnO, the increase of charge density between the Zn ions leads to stronger bonding between them. The decrease in Zn-Zn distance from 2.60 Å in pristine $(\text{ZnO})_{12}$ cluster to 2.54 Å in Mg doped cluster supports this argument. From a simple tight-binding model of the cluster, this leads to an increase in the off-diagonal matrix elements of the Hamiltonian and therefore the HOMO-LUMO gap, which is essentially the energy difference between bonding and anti-bonding states increases. In Cd doped ZnO, the charge between Zn ions deplete, leading to a weakening of bonding between them. The Zn-Zn distance in this case increases to 2.64 Å, indicating lower overlap between tight-binding basis orbitals and thus reduction in HOMO-LUMO

gap.

The variation of band gap with Mg/Cd doping can also be explained on the basis of electronegativity difference between X (X=Mg, Zn, Cd) and O atoms. The electronegativity difference between Mg and O is the largest and that between Cd and O is the smallest. The X-O bonds are partially ionic and partially covalent. If we relate the ionicity of the X-O bond to the electronegativity difference between X and O, then MgO should be the most ionic and CdO the least with ZnO in the middle. The trend of increase in band gap in Mg doped ZnO and decrease in band gap in Cd doped ZnO is thus consistent with the ionicity theory of Phillips [54], Nelson and Batra [55], and Catlow and Stoneham [56].

4.3 Summary

We have studied the band gap variation in Mg/Cd doped nanostructures and small clusters of ZnO. We have shown for the first time the tailoring of energy gap in ZnO clusters of sizes less than 1 nm. The energy gap of both clusters and nanostructures of ZnO increases with Mg doping while it decreases with Cd doping. The variation of HOMO-LUMO gap in Mg/Cd doped ZnO clusters follows the similar trend of variation of band gap in Mg/Cd doped nanostructures. We have explained this behaviour on the basis bonding character and ionicity. The energetics results show that Mg doping is energetically more favorable than Cd doping. The stability of ZnO cluster increases with Mg doping while it decreases with Cd doping.

Chapter 5

Magnetism in Cr doped ZnTe clusters

In this chapter we study magnetic properties of Cr doped ZnTe clusters¹. As bulk and thin films of Cr doped ZnTe have emerged as promising spintronic materials, we aim here to investigate the magnetic behaviour of Cr doped ZnTe in the regime of cluster. We have studied the energetically favorable doping sites for Cr in ZnTe host as well as the nature of coupling between Cr atoms.

5.1 Introduction

Ever increasing trend in device miniaturization has prompted extensive research in low dimensional systems [57]. The gas phase clusters exhibiting magnetism are considered as potential candidate materials in data storage technology [58, 59]. The reduction of dimension from bulk to nano-scale often gives rise to novel physical properties. For example, 4-*d* elements like Ru, Rh, Pd which are non-magnetic in bulk phase have been found to exhibit magnetism in the regime of small clusters [60, 61]. Similarly, due to quantum confinement effect, small clusters of metal exhibit energy gap between HOMO and LUMO. Moreover, the properties of clusters vary with the size and composition and thus clusters of desirable properties can be synthesized by controlling these parameters.

¹This chapter is based on the paper : *Structural, electronic and magnetic properties of (ZnTe)₁₂ clusters*, J. Magn. Magn. Mater. **321** (2009); **Manoj K Yadav**, Biplab Sanyal and Abhijit Mookerjee.

While there are several studies for magnetism in metallic and bimetallic clusters, the study of magnetism in semiconductor clusters remains less explored. Nayak *et al.* [62] have reported the occurrence of ferromagnetism in MnO clusters despite the fact that the bulk MnO is a strong AFM system. Liu *et al.* [63] have studied magnetic properties of Mn doped ZnO clusters. They have studied the nature of magnetic coupling between Mn atoms at different distances. They found anti-ferromagnetic coupling for smaller Mn-Mn separation while for larger Mn-Mn separation the AFM state was found to be degenerate with FM state. Das *et al.* [64] have carried out density functional based study on Cr doped small clusters of $(\text{GaN})_n$ for $n=1, 2$ and 3 . They have reported that ferromagnetic coupling between Cr atoms in these clusters are favorable over antiferromagnetic ones. We have studied the magnetic properties of Cr doped $(\text{ZnTe})_{12}$ clusters through first principles calculations. The motivation is driven from the following promising reports:

- (1) Cr doped thin film [65] and bulk [66] ZnTe have been found to exhibit room temperature ferromagnetism,
- (2) Ferromagnetism in Cr doped bulk ZnTe is more stable than other TMs (Mn, Fe, Co) doped ZnTe [67], and
- (3) Bulk ZnTe can be doped with fairly large concentration of TMs [68].

The structural and electronic properties of small clusters of pristine $(\text{ZnTe})_n$ for $n \leq 9$ have been studied earlier by Matxain *et al.* [26]. They found planar ground state structures for $n \leq 5$ and three dimensional cage-like ground state structures for $n \geq 6$, with $n=7$ being an exception. The cage-like structures are made up of units of rhombi and hexagons. With our earlier experience from ZnO clusters (Chapters 3 and 4), we have chosen ZnTe cluster consisting of 12 ZnTe units for Cr doping. As in the case of $(\text{ZnO})_{12}$ here also we found cage like ground state for $(\text{ZnTe})_{12}$ cluster. It is made up with units of rhombi and hexagons, and resembles $(\text{ZnO})_{12}$ cluster. It is highly symmetric and has a large

HOMO-LUMO gap (2.34 eV), and therefore should be a suitable candidate for doping. Moreover our calculation suggests that binding energy of $(\text{ZnTe})_{12}$ cluster increases on doping with Cr atom. Such enhancement of binding energy is one of the prerequisites for a cluster to be a candidate for the synthesis of cluster assembled solids.

5.2 Computational Details

First principles density functional theory based calculations have been carried out under PAW scheme [18, 19]. The exchange correlation energy is calculated using PBE functional [12]. The pseudo-potentials of Zn, Te and Cr atoms were generated by including their d electrons in the valence configuration. The clusters were placed in a super-cell whose size was large enough (cube of sides $\sim 15 \text{ \AA}$) to avoid interaction between periodic images of the clusters. Single point (Γ) calculations have been carried out with plane wave cut off of 276.7 eV. The geometries of the clusters have been optimized using the conjugate gradient algorithm and the convergence was achieved till the Hellman-Feynman force on each ion was less than 0.01 eV/\AA .

5.3 Results and Discussion

5.3.1 Pristine $(\text{ZnTe})_{12}$ clusters

First we study the structure and stability of pristine $(\text{ZnTe})_{12}$ clusters which will be helpful in analyzing the properties of doped $(\text{ZnTe})_{12}$ clusters. In order to investigate the ground state structure of $(\text{ZnTe})_{12}$ several starting geometries including the bulk like zinc blende structure were considered. The ground state structure (labeled as GS) and the two closest local minimum structures (labeled as LM1 and LM2) of $(\text{ZnTe})_{12}$ are shown in Fig. 5.1. The GS is a highly symmetric cage-like structure. Such cage-like structure has also been found to be the ground state for $(\text{ZnO})_{12}$. It consists of six rhombi and eight

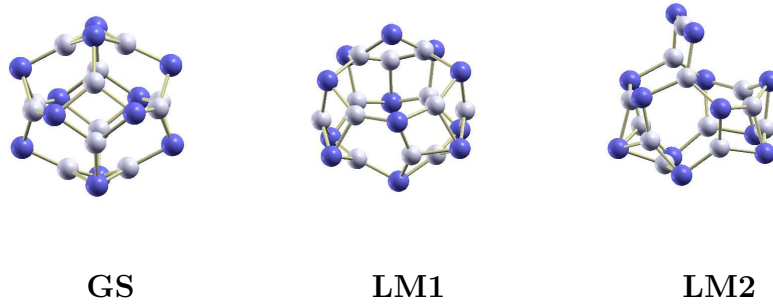


Figure 5.1: Ground state (GS) and local minima (LM1 and LM2) structures of pristine $(\text{ZnTe})_{12}$ clusters. White spheres represent Zn atoms and darker spheres represent Te atoms.

hexagons, and appears like a C_{60} fullerene (which, in contrast, has units of pentagons and hexagons). There are two types of Zn-Te bonds, a shorter one (2.57 \AA) connecting two neighbouring rhombi and a larger one (2.64 \AA) connecting a Zn atom and a Te atom in the same rhombus. The diameter of the cage (as measured between the two farthest Te atoms) is about 0.87 nm .

The calculated binding energies per atom of GS, LM1 and LM2 are 2.07, 2.01 and 1.98 eV, respectively. Thus, the ground state structure is energetically favourable over the next higher energy structure by about 1.44 eV indicating its higher relative stability. The binding energy per unit ZnTe of GS is about 4.14 eV which is less than the corresponding bulk phase value of 4.82 eV suggesting the generally expected result that the clusters are energetically less favourable than the corresponding bulk phase. The HOMO-LUMO gaps in GS, LM1 and LM2 are 2.34, 1.43 and 1.42 eV respectively. The large HOMO-LUMO gap of GS reflects its greater stability. The HOMO-LUMO gap of GS may be compared with the value of the band gap of 2.26 eV for bulk ZnTe in zinc blende structure. The qualitative aspect of increase in energy gap in clusters due to quantum confinement effect is clearly reflected, but quantitative estimate will certainly be erroneous due to the limitation of ground state DFT. Akin to nonmagnetic bulk ZnTe, all the pristine $(\text{ZnTe})_{12}$ clusters

shown in Fig. 5.1 are closed shell systems without any local atomic magnetic moment.

5.3.2 Monodoped clusters

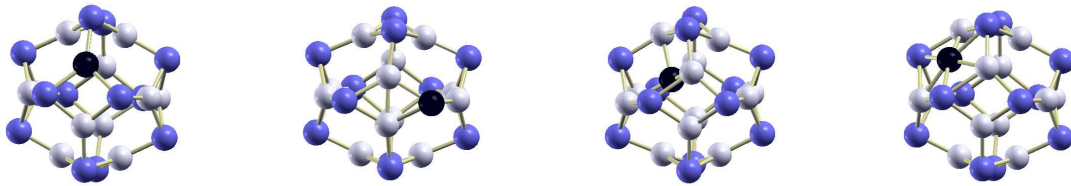


Figure 5.2: Optimized structures of mono-doped clusters, (Left to Right) M1, M2, M3 and M4. Dopant Cr atoms are represented by black spheres and colour codes of Zn and Te atoms are same as in Fig. 5.1.

First we study the structural, electronic and magnetic properties of ground state $(\text{ZnTe})_{12}$ cluster doped with single Cr atom. We study four different kinds of mono-doping cases:

- (i) a Zn atom substituted by a Cr atom,
- (ii) a Te atom substituted by a Cr atom,
- (iii) a Cr atom placed inside cage and
- (iv) a Cr atom placed outside cage over a hexagonal unit.

These are indicated, respectively, as M1, M2, M3 and M4 in Fig. 5.2. For all doping cases we consider only the ground state structure.

The structures M1 and M2 are similar to pristine $(\text{ZnTe})_{12}$ clusters with some local changes in bond lengths. The Cr-Te distance in M1 is 2.77 \AA which is larger than Zn-Te distance in pristine $(\text{ZnTe})_{12}$ cluster. In the case of M3, the Cr atom initially placed at

Table 5.1: Binding energy per atom, E_b in eV, formation energy, E_{form} in eV, HOMO-LUMO gap (smallest of the two spin channels), E_{gap} in eV and magnetic moments in Bohr-magneton (μ_B) of the mono-doped clusters.

Cluster	E_b	E_{form}	E_{gap}	Magnetic moment	
				Cr	Total
M1	2.089	-0.521	0.58	3.75	3.62
M2	1.914	3.691	1.00	4.07	3.80
M3	2.026	-1.031	1.36	4.29	4.66
M4	2.007	-0.560	0.64	4.04	4.62

the middle of the cage moves just below a hexagonal surface after geometry optimization. Similarly, in the case of M4, the Cr atom placed outside the cage moves a little above the hexagonal surface. Apart from formation of new Cr-Zn and Cr-Te bonds due to inclusion of a Cr atom, the other bond lengths in M3 and M4 remain more or less similar to those in the parent pristine $(\text{ZnTe})_{12}$ cluster.

The binding energy per atom, defect formation energy², HOMO-LUMO gaps, magnetic moment of Cr atom and total magnetic moment of all these mono-doped clusters are shown in Table 5.1. The cluster M1 has the largest binding energy per atom. M2 is higher in energy than M1 showing that Cr doping at Zn site is more favourable than Cr doping at Te site. This behaviour is further supported by defect formation energy. The lower defect formation energy for Cr doping at Zn site than that at Te site implies that it is easier to dope Cr atom at Zn site. Comparing the energetics of M3 and M4 it is clear that endohedral doping is more feasible than the exohedral doping.

All Cr doped clusters have significant magnetic moments, mainly contributed by the 3- d orbitals of Cr atom. This result is totally different from Cr doped Si_{16} cluster where the moment of Cr atom is completely quenched [69]. The magnitude of the total magnetic moments are ordered in the four clusters as $M1 < M2 < M4 < M3$. Te atoms in cluster M1

²The procedure for the calculation of formation energy has been outlined in Chapter 4

carry small induced magnetic moments ($\sim 0.06 \mu_B$) which are antiparallel to the moment on Cr atom. The smaller the Cr-Te distance, the more is the hybridization of the 3d states of TM with the states of Te resulting in smaller total magnetic moment. The magnetic moment ordering $M1 < M2$ agrees this behaviour as Cr atom in M1 is coordinated with 3 Te atoms while in M2, the Te atoms lie farther away. However in the case of M3 and M4, Zn as well as Te atoms have small induced moments parallel to the moment of Cr and thus resulting in enhancement of total magnetic moment in these clusters. The large local magnetic moment on Cr atom in M3 is due to extra contribution from Cr-*s* ($0.15 \mu_B$) and Cr-*p* ($0.09 \mu_B$) states. The local magnetic moment of Cr atom in all cases is found to be larger than the values obtained from similar calculations for Cr doped bulk [71] and thin film [72] of ZnTe. This is mainly because of reduced coordination found in the clusters.

5.3.3 Bi-doped clusters

In this section we study the nature of magnetic coupling between two Cr atoms in $(\text{ZnTe})_{12}$ cluster. As the binding energy and formation energy results in previous section favour Cr substitution at Zn sites than that at Te sites all the subsequent calculations have been carried out for Cr doping at Zn sites only. We have chosen three different combinations of Zn sites for Cr substitution :

- (i) opposite vertices of a rhombus,
- (ii) adjacent Zn sites in a hexagon and
- (iii) Zn-sites of two unconnected hexagons such that Zn-Zn distance is the farthest apart as shown in Fig. 5.3.

These are labeled in the order of increasing Cr-Cr distance as BF1, BF2 and BF3, respectively, for ferro-magnetically coupled Cr atoms. The corresponding clusters with

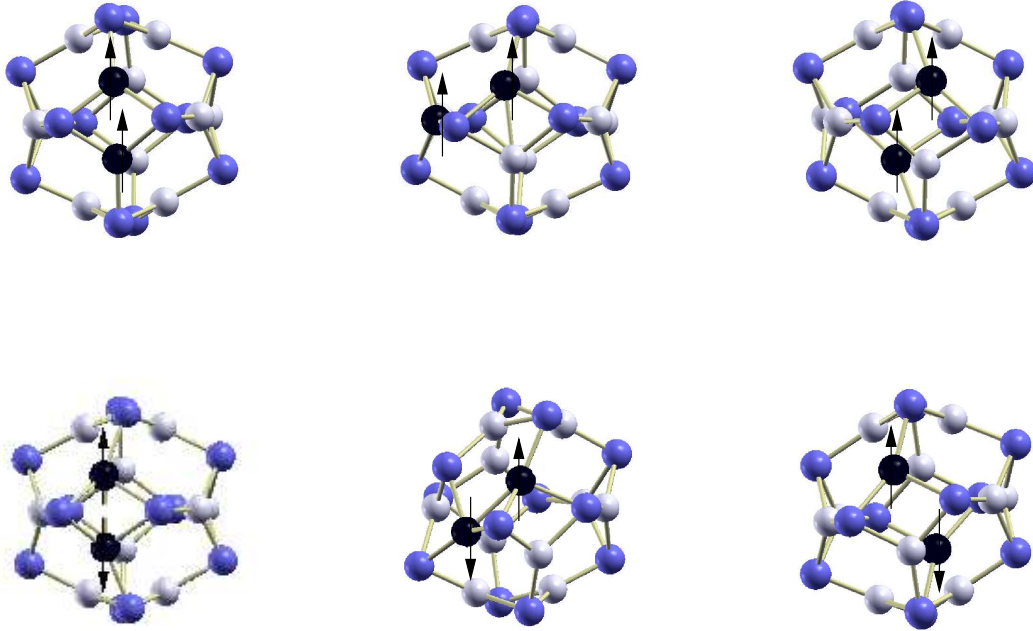


Figure 5.3: Optimized structures of bi-doped $(\text{ZnTe})_{12}$ clusters: (Top) BF1, BF2 and BF3 (Bottom) BAF1, BAF2 and BAF3. Colour codes of atoms are the same as in Fig. 5.2. The parallel and antiparallel arrows indicate FM and AFM couplings respectively.

antiferromagnetically coupled Cr atoms are labeled as BAF1, BAF2 and BAF3 respectively.

The results for bi-doped clusters are listed in Table 5.2. Except for the local deformation, the geometrical structures of BF1, BF2 and BF3 are similar to that of the pristine $(\text{ZnTe})_{12}$ cluster. However, the structures of clusters with antiferromagnetically coupled Cr atoms, particularly BAF1 and BAF2, are significantly distorted. This is evident from the huge reduction in the distance between two Cr atoms, $d_{\text{Cr-Cr}}$ in BAF1 and BAF2.

The cluster BF1 is found to be the ground state configuration. The energy ΔE in the Table 5.2 is the energy of clusters with respect to the energy of this ground state configuration. Comparing the energetics of ferromagnetic arrangement BF1 with the

Table 5.2: Distance between Cr atoms, $d_{\text{Cr-Cr}}$ in Å, energy difference with respect to BF1, ΔE in eV, binding energy, E_b in eV/atom, and magnetic moments in units of Bohr-magneton (μ_B).

Cluster	$d_{\text{Cr-Cr}}$	ΔE	Magnetic moment	
			Cr atom	Total
BF1	2.96	0.0	3.76	7.25
BF2	3.40	0.144	3.74	7.23
BF3	6.83	0.240	3.75	7.29
BAF1	2.82	0.072	3.53	0.00
BAF2	2.91	0.024	3.56	0.02
BAF3	6.82	0.242	3.75	0.00

corresponding antiferromagnetic ones it is clear that ferromagnetic arrangement BF1 is favourable over the AFM arrangement BAF1 by about 36 meV energy per Cr atom. The clusters BF3 and BAF3 are degenerate in energy which suggests that there is no long range coupling between two Cr atoms. This is further supported by the fact that there is no appreciable difference in Cr-Cr distance and also the magnitude of local magnetic moment of Cr atom in both BF3 and BAF3 is the same. The only case favoring anti-ferromagnetic arrangement is BAF2. The significant decrease in Cr-Cr distance (14.4 %) in BAF2 suggests strong Cr-Cr magnetic coupling in the AFM state. This indicates the tendency of Cr_2 anti-ferromagnetic dimer formation. In fact Cr_2 free dimer is found to be antiferro-magnetically coupled [73]. In order to investigate the effect of Cr-Cr distance we performed static calculation for BAF2 keeping Cr-Cr distance equal to the case of BF2 (3.40 Å). In this case BAF2 comes to be less favorable than BF2 by about 0.08 eV. However, the Cr-Cr distance itself cannot be fully responsible for this, for if it were so then BAF1 would also be favorable over BF1. The more important factor seems to be the local environment. In the case of BF1 there lies two Te atoms in between two Cr atoms whereas in the case of BF2 (or BAF2) there is only one Te atom in between two Cr atoms.

Comparing the magnetic moments in bidoped clusters with that in M1, we find that the ferromagnetic configurations more or less retain the magnetic moment of Cr atom in M1. The magnetic moment of Cr atom is significantly reduced in BAF1 and BAF2. This is because of larger proximity of Cr atoms in BAF1 and BAF2 causing Cr $d-d$ hybridization.

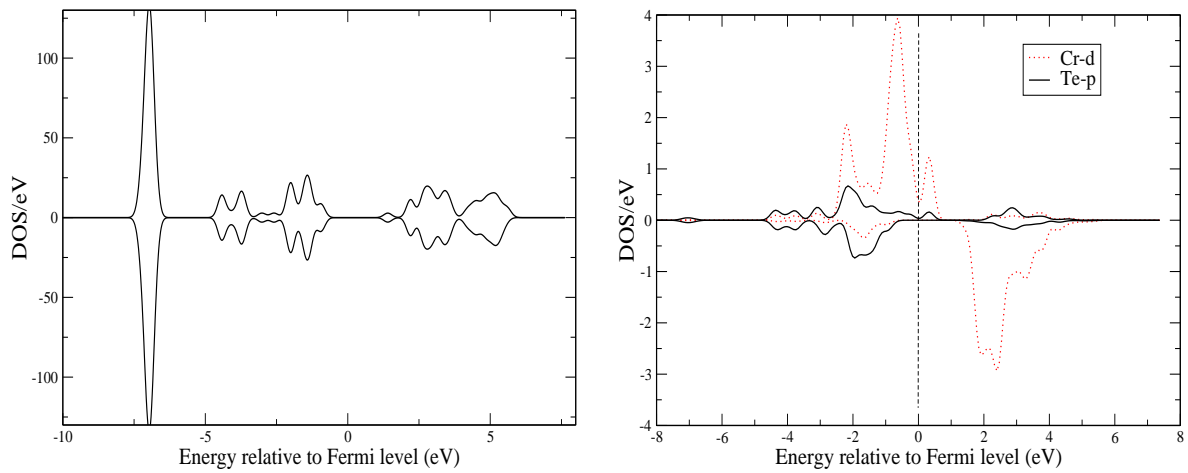


Figure 5.4: (Left) Total DOS of undoped $(\text{ZnTe})_{12}$ cluster and (Right) atom projected partial DOS of Cr- d and Te- p states of the mono-doped $(\text{ZnTe})_{12}$ cluster, M1. The dashed vertical line is the Fermi level (shifted to 0 eV). Majority (up) spin states are plotted along positive y axis and minority (down) spin states along negative y axis.

Finally, we study the density of states (DOS) of undoped and doped clusters to analyze the effect of Cr doping over evolution of magnetism. The total DOS of pristine $(\text{ZnTe})_{12}$ cluster is shown in the left panel of Fig. 5.4. There is no spin polarization which shows the non-magnetic nature of the $(\text{ZnTe})_{12}$ cluster like the bulk ZnTe. The right panel of Fig. 5.4 shows the atom projected partial DOS of mono-doped cluster M1. The dotted line is for Cr- d states and the solid line is for Te- p states. The magnetic moment in M1 mainly comes from the polarized Cr- d states. As the Cr atom is sitting at Zn site in 2^+ state, one would expect the moment of $4 \mu_B$ on it. But, the hybridization between Cr- d

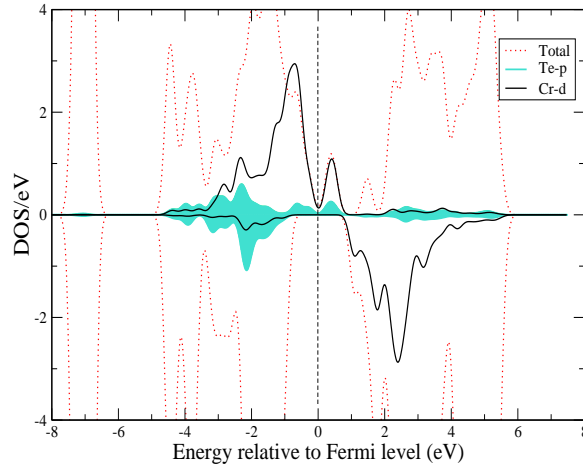


Figure 5.5: Partial DOS of Cr $3d$ and Te $5p$ states in the cluster BF1. Total DOS is also plotted which is scaled down for the sake of clarity. The dashed vertical line is the Fermi level (shifted to 0 eV). Majority (up) spin states are plotted along positive y axis and minority (down) spin states along negative y axis.

and Te- p causes the reduction in the moment. The Cr induced states falls in the gap causing the narrowing of HOMO-LUMO energy gap.

Next we study the DOS of bi-doped cluster BF1 to explore the origin of ferromagnetic coupling in it. To serve this purpose we plot partial DOS of Cr $3d$ and Te $5p$ states in Fig. 5.5. Substantial amount of Cr- d states can be seen above Fermi level. These d states tend to align parallel to the d states of another Cr atom and thus effectively leading to ferromagnetic coupling between the two Cr atoms. This is ferromagnetic superexchange mechanism. The possibility of ferromagnetic superexchange is also supported by close to 90° Cr-Te-Cr angle in BF1. However, there is also strong $p-d$ hybridization leading to shift of $p-d$ hybridized states to higher energy side in up spin channel and to lower energy side in down spin channel. Thus Zener's $p-d$ exchange mechanism [70] also seems contributing to stabilization of the ferromagnetic state. There is absence of down spin states at the Fermi level, thus the ferromagnetism is of half metallic nature. This agrees with earlier reports of occurrence of half metallic ferromagnetism in Cr doped bulk [71]

and thin film [72] of ZnTe.

5.4 Summary

We found highly symmetric cage-like structure for $(\text{ZnTe})_{12}$ clusters. The substitutional doping of Cr atom at Zn site is found to be the most favorable. Monodoped clusters show atomic like magnetic moment. In the case of bidoped clusters, both ferromagnetic and anti-ferromagnetic exchange coupling are found to exist depending on the local environment around Cr atoms. The ferromagnetic state is more stable when two Cr atoms lie on opposite vertices of a rhombus. The ferromagnetism is of half metallic nature. Antiferromagnetic state is favourable when two Cr atoms lie at the adjacent Zn sites of a hexagon. When Cr atoms are farthest apart both ferromagnetic and antiferromagnetic states are found to be degenerate indicating that the magnetic exchange coupling in between Cr atoms is short ranged.

Chapter 6

Ferromagnetism in Mn doped and C co-doped ZnO

In this chapter we shall discuss the magnetism in Mn doped bulk ZnO¹. Mn doped ZnO is found to be an antiferromagnetic system. We co-dope ZnMnO with carbon which provides holes into the system. We show that carbon concentration as low as about 2.8 at. % can lead to stabilization of ferromagnetic state in ZnMnO.

6.1 Introduction

After the theoretical prediction by Dietl *et al.* [74] suggesting the occurrence of room temperature ferromagnetism (RTF) in Mn doped ZnO and GaN, these systems have been studied extensively. While the initial DMS perspective research was focused to doped GaN, recently ZnO has attracted much attention as it is easier to synthesize its single crystals [75]. The solubility limit of Mn into ZnO is fairly large [76], which is another important advantage over GaN. However, the occurrence of ferromagnetism as well as its physical origin in transition metal doped ZnO is controversial. The RTF in bulk as well as thin film of $Zn_{1-x}Mn_xO$ has been reported by Sharma *et al.* [45]. Pradhan *et al.* have also reported RTF in pulsed-laser deposited epitaxial thin film of ZnMnO [77]. Contrary to these reports, there are several studies showing the absence of ferromagnetism in TM

¹This Chapter is based on the Paper: *Stabilization of ferromagnetism in Mn doped ZnO with C co-doping*, J. Magn. Mater. **321**, 273 (2009); **Manoj K Yadav**, Biplab Sanyal and Abhijit Mookerjee.

doped ZnO [78, 79, 80]. Ueda *et al.* [78] prepared 3-*d* transition metal doped ZnO thin film using pulsed laser deposition method. They reported absence of ferromagnetism in Cr, Mn and Ni doped films. Similarly the works by Jin *et al.* [79] and Lee *et al.* [80] do not show the occurrence of ferromagnetism in Cr doped ZnO thin film, and the need for co-doping (to introduce carriers) has been suggested for making the system ferromagnetic [80, 81, 82]. Experimental study [83] as well as first principle calculation [84] shows the stabilization of ferromagnetism in ZnCoO when co-doped with Al. The *ab initio* calculation by Sato *et al.* [85] also shows the stabilization of ferromagnetic state in ZnMnO by introducing holes.

We explore the possibility of ferromagnetism in Mn doped ZnO. Doping ZnO by Mn at Zn site is isovalent doping, i.e Mn does not provide any carrier into the system. In the absence of any carrier the coupling between two Mn atoms is dominated by anti-ferromagnetic superexchange mechanism. As depicted by some earlier studies [84, 85] that introduction of external carriers by co-doping leads to the stabilization of ferromagnetic state in otherwise anti-ferromagnetic systems, we show on the basis of *ab initio* calculation that ferromagnetic state can be stabilized in ZnMnO when co-doped with C atom at O site.

6.2 Computational Details

The calculations were carried out using a plane wave based DFT code, namely the Vienna *ab initio* simulation package (VASP). The electron-ion interactions have been described by PAW method [18, 19] which is specially suitable for proper treatment of semi-core electrons of transition metals. The exchange correlation energy is calculated using PBE functional [86]. The pseudo potentials for Mn and Zn were generated by including their 3-*d* states in the valence configuration. The calculations were performed using a $3 \times 3 \times 2$ super-cell consisting of 36 formula units of ZnO. The choice of such a large super-cell helps to keep

the dopant concentration close to practical limit and also avoids the spurious magnetic interaction between a magnetic dopant and its image. A Γ centered $3 \times 3 \times 2$ Monkhorst-Pack mesh was used for the integration of charge densities over the Brillouin zone. The plane wave cut off energy was set to 400 eV. All the atoms in the super-cell were relaxed till the Hellman-Feynman force on each ion was less than 0.01 eV/Å.

6.3 Results and Discussion

Two nearest neighbour coplanar Zn atoms were replaced by Mn atoms as shown in Fig.6.1. This corresponds to 5.55 at.% of doping. Total energy calculations for ferromagnetic (FM) and anti-ferromagnetic (AFM) couplings show that AFM state is energetically favourable over FM state by about 34 meV/Mn atom. Thus in the absence of any external carrier the coupling between Mn atoms in ZnO matrix is AFM. This result is in agreement with the Korringa-Kohn-Rostoker (KKR) method based LDA calculation by Sato and Katayama-Yoshida [85], Iusan *et al.* [87] and Rosa and Ahuja [88].

In order to introduce some carriers into the system we co-dope ZnMnO with carbon atom at O site. Carbon has two electrons less than that of oxygen and hence it introduces two holes into the system. The formation energy for such doping was found to be 3.21 eV which shows that there is a reasonable possibility of such a doping. In order to have an idea about site preference of C atom and hence its effect on magnetic coupling between the Mn atoms, we dope a C atom at three different O sites, marked as **1**, **2** and **3** in Fig. 6.1, hence forth known as configurations **1**, **2** and **3** respectively. The choice of such sites ensures that the C atom remains equidistant from both Mn atoms in each case.

For each configuration total energy calculations were carried out for both the FM and AFM couplings between the two Mn atoms. The results are listed in Table 6.1. The configuration **1** in the FM state is found to be the minimum energy configuration. The energy ΔE in Table 6.1 is the energy relative to the energy of the configuration **1** in FM

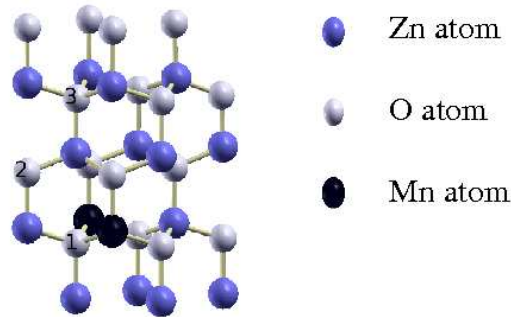


Figure 6.1: A portion of the 72-atom super-cell showing Mn and C doping sites. Three different C doping sites are marked as 1, 2 and 3.

state. The FM state in configuration **1** is stable over its AFM state by about 0.34 eV/Mn. Thus there is huge difference in energy showing the stabilization of ferromagnetic state. It should be noted that in the absence of co-doping by C atom, AFM state was stable over FM state by only about 0.068 eV. Such a remarkable reversal in magnetic coupling is brought about by co-doping with a single C atom which is equivalent to only about 2.8 at. % doping. The highly stable FM state indicates the possibility of large transition temperature. Moreover, the transition temperature can be controlled by adjusting the concentration of carbon doping.

The magnetic moments on the Mn atoms for both FM and AFM couplings in configuration **1** are $3.46 \mu_B$ and $3.33 \mu_B$ respectively. Thus the presence of C atom leads to the reduction in magnetic moments in both cases. This is because Mn-C distance (1.86 Å) is much smaller than Mn-O distance (2.01 Å) which causes strong $p-d$ hybridization resulting in reduction of the magnetic moment. This will be evident while analyzing atom projected density of states (Fig. 6.3) later. The distance, d_{Mn-Mn} between the two Mn atoms heavily reduces in the case of FM coupling but remains more or less the same in the case of AFM coupling.

Table 6.1: Relative energy ΔE in eV, Magnetic moment of Mn in μ_B , distance between Mn atoms, d_{Mn-Mn} in Å, and distance between Mn and C atoms, d_{Mn-C} in Å for configurations **1**, **2** and **3**.

Config- uration	Magnetic state	ΔE	Magnetic moment of Mn	d_{Mn-Mn}	d_{Mn-C}
1	FM	0.00	3.48	3.17	1.86
	AFM	0.68	3.33	3.24	1.89
2	FM	2.34	4.05	3.29	3.83
	AFM	2.33	4.04	3.28	3.82
3	FM	2.19	4.01	3.29	5.09
	AFM	2.23	3.98	3.25	5.07

The FM and AFM state in configurations **2** and **3** are almost degenerate. C atom in these configurations lie much farther from the Mn atoms. However, it can interact with Mn atoms indirectly through the neighbouring Zn and O atoms. This is evident from the fact that neighbouring Zn and O atoms which otherwise are nonmagnetic now carry significant magnetic moments ($0.01-0.09\mu_B$). However, this interaction is weak and the FM state is not stabilized. The energetics of configurations **2** and **3** show that these are energetically highly unfavorable configurations compared to the configuration **1**. This implies that during synthesis of ZnMnO:C, carbon atom will tend to reside closer to Mn atoms. Incidentally, FM state is highly stable when C atom is close to Mn atoms (configuration **1**).

Let us first analyze the density of states in the absence of C co-doping. The spin polarized partial density of states of Mn d and O p (of O atom at site 1) for AFM state is shown in Fig. 6.2. Mn atoms sit at Zn sites in 2^+ state and hence they assume d^5 high spin configuration. Thus up spin d states are fully occupied and down spin d states are fully empty (slightly unoccupied d states appearing just above the Fermi level is due to smearing width (0.1 eV) used in the calculation). There is absence of carriers in the

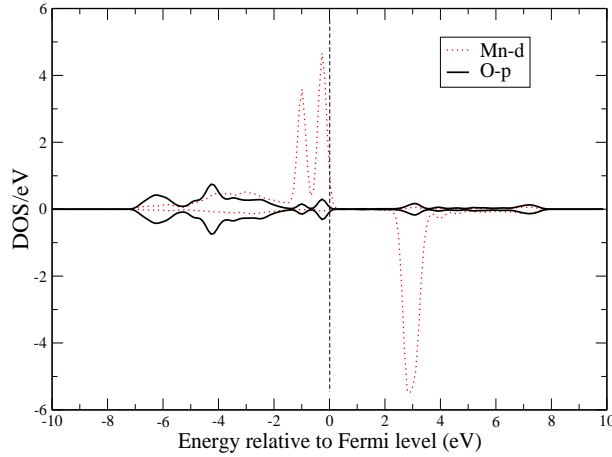


Figure 6.2: Density of states of Mn- d and O- p for the AFM state of Mn doped ZnO. The dashed vertical line indicates the position of the Fermi levels (shifted to 0 eV). Majority (up) spin states are plotted along positive y axis and minority (down) spin states along negative y axis.

system. In this case the coupling between two Mn atoms is mediated by spin polarized moments on intermediate O atom. The spin up O $2-p$ states couple with spin up d states of one Mn atom, while spin down O $2-p$ states couple with spin down d states of another atom. This is typical of antiferromagnetic superexchange [89, 90] coupling which leads to lowering the energy in the AFM state by pulling the d states toward lower energy side.

Now we analyze the DOS of carbon co-doped ZnMnO. The spin polarized DOS of Mn d states and C p states for configuration **1** in FM state is shown in Fig. 6.3. There is presence of strong $p-d$ hybridized hole states at the Fermi level. This causes partial occupancy in Mn d states. A $3-d$ electron from a partially occupied d states of one Mn atom can hop to a partially occupied $3-d$ orbital of the neighbouring Mn atom, provided the neighbouring Mn atom has parallel spin. Thus, the kinetic energy is lowered if the two Mn atoms are ferro-magnetically coupled. This is the double exchange mechanism [91] which wins here over the AFM superexchange mechanism. We also notice highly delocalized d states hybridizing with the valence band p states resulting in polarization of

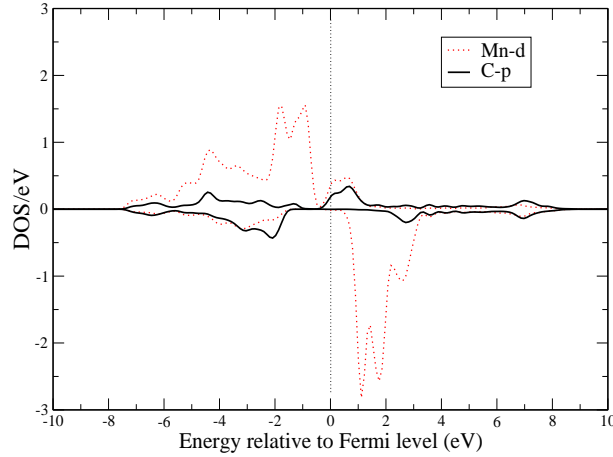


Figure 6.3: DOS of Mn- d and C- p for the FM state of carbon co-doped ZnMnO. The dashed vertical line indicates the position of the Fermi level (shifted to 0 eV).

p states. This leads to pushing the up spin p states to higher energy side and down spin p states to lower energy side which effectively results in lowering in energy. Thus, the $p - d$ exchange mechanism [70] is also contributing in stabilizing the ferromagnetic state. This situation of simultaneous presence of both double and $p - d$ exchange mechanisms is also seen in Mn doped phosphides and arsenides of aluminium and indium [92].

6.4 Summary

We have presented first principles study of magnetism in ZnMnO. The coupling between Mn atoms in ZnMnO is found to be antiferromagnetic which is expected results in the absence of external carriers. We introduced carriers (holes) into the system by co-doping with C atoms. We found that the concentration of C atom as low as about 2.8 at. % leads to the stabilization of ferromagnetism. The ferromagnetic state is stabilized due to both double and $p - d$ exchange mechanisms. Since the FM state is stabilized due to introduction of holes into the system, the concentration of hole provides a tool to control the transition temperature.

Chapter 7

Tuning ferromagnetism in manganese oxide

In this chapter we show how an anti-ferromagnetic semiconductor MnO can be converted to a ferromagnetic one¹. This work is motivated from the result of the previous chapter where we showed the stabilization of ferromagnetism in ZnMnO by introducing holes into it. Here we apply the same idea to the anti-ferromagnetic semiconductor MnO. We show that doping MnO by 2-*p* elements like C and N, introduces holes into the system leading to ferromagnetic ordering in MnO.

7.1 Introduction

The magnetic oxides, MO (M = Mn, Fe, Co, Ni) in the rock salt structures are well known anti-ferromagnetic materials owing to M-O-M anti-ferromagnetic super-exchange mechanism. Among these, MnO is the highest local magnetic moment ($5\mu_B$) bearing material with transition temperature of 118 K [93], and can be considered as a model system for theoretical understanding of electronic and magnetic properties in rock salt MO [94, 95]. MnO being a semiconductor with large band gap (3.6-3.8) [96] can be a good candidate for spintronic applications if spontaneous magnetization is achieved in it.

Unlike the conventional approach of achieving ferromagnetism in a semiconductor by

¹This chapter is based on the paper: *Tuning magnetism of MnO by doping with 2p elements*, J. Magn. Magn. Mater. (accepted); **Manoj K Yadav**, Abhijit Mookerjee and Biplab Sanyal.

doping it with few concentration of a 3-*d* element [97, 98], some studies [99, 100, 101] suggest that doping by a 2-*p* element can also bring about ferromagnetism. Bannikov *et al.* [99] have reported the occurrence of half metallic ferromagnetism in MgO by doping with 2-*p* elements like B, C, N. Half metallic ferromagnetism is also found in carbon doped SrO and BaO [102]. Wu *et al.* [100] have achieved spontaneous magnetization in BN nanotubes by carbon substitution for either a boron or a nitrogen atom. A recent study by Gorbunova *et al.* [101] shows that the non-magnetic BeO nanotube can be converted to magnetic one by doping with B, C, N at O site. All the aforesaid studies pertain to achieving ferromagnetism in nonmagnetic systems. In this chapter we explore the role of 2-*p* elements in the anti-ferromagnetic semiconductor, MnO. We show with the help of *ab initio* calculations that ferromagnetism can indeed be achieved in MnO by doping it with carbon and nitrogen at oxygen sites.

7.2 Computational Details

First principles density functional calculations have been performed using the PAW based method implemented in VASP code [18, 19, 105]. The generalized gradient spin density approximation to the exchange correlation functional has been employed within the PBE scheme [12]. The strong on-site Coulomb repulsion of 3-*d* states of Mn has been accounted under Dudarev scheme [103] using $U-J=6$ eV, where U and J are the Coulomb and exchange parameters in the Hubbard model. To facilitate small doping concentration a 64 atom super-cell has been used. The Brillouin zone sampling has been done with $4\times 4\times 4$ Monkhorst-Pack k-point grid. The plane wave energy cut off of 500 eV resulted in a good convergence. Full geometry optimizations were done using conjugate gradient algorithm with Hellman-Feynman force convergence threshold of 0.01 eV/Å.

For MnO in type II anti-ferromagnetic state [Fig. 7.1], the above computational set-up resulted in lattice parameter of 4.50 Å, rhombohedral distortion angle of 0.56°, the local

spin magnetic moment for Mn atom of $4.69\mu_B$ and the band gap of 2.02 eV. All these values agree well with the similar PBE+U calculation by Franchini *et al.* [104]. The type II antiferromagnetic ordering in MnO is lower in energy (by about 7 meV/Mn atom) than type I ordering (alternate 100 planes with opposite spin polarizations), and therefore we considered only type II ordering for subsequent calculations.

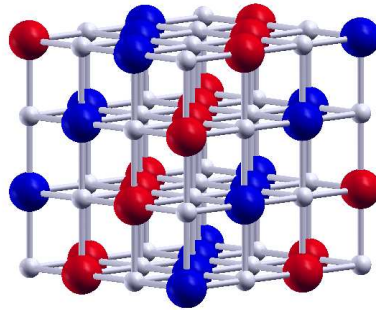


Figure 7.1: Type II AFM ordering in MnO. Red spheres represent spin up Mn atoms and blue spheres spin down Mn atoms. Small white spheres represent O atoms.

7.3 Results and Discussion

First we investigate the favorable substitutional site for X (C and N) by calculating formation energies when X is substituted at Mn and O sites. The expressions for formation energies at Mn and O sites are respectively given by

$$E_f[Mn] = E[Mn_{31}XO_{32}] - E[Mn_{32}O_{32}] - \mu_X + \mu_{Mn}, \quad (7.1)$$

and

$$E_f[O] = E[Mn_{32}XO_{31}] - E[Mn_{32}O_{32}] - \mu_X + \mu_O, \quad (7.2)$$

where $E[Mn_{32}O_{32}]$ is the energy of the undoped super-cell and $E[Mn_{31}XO_{32}]$ and $E[Mn_{32}XO_{31}]$ are the energies of super-cell with X doped at Mn and O sites respectively. μ_X , μ_{Mn} and

μ_O are the chemical potentials of X, Mn and O respectively. The chemical potentials for Mn and C were calculated with reference to their bulk stable phases (alpha-Mn and graphite) whereas the chemical potentials of N and O were calculated with reference to their stable molecular configurations. The calculated values for chemical potentials of Mn, O, N and C are 5.926, 4.929, 8.312 and 9.212 eV respectively. The formation energy for C and N substitution at Mn site are 9.499 and 10.062 eV respectively. The corresponding values for substitution at O site are 6.605 and 4.130 eV respectively. As expected, the doping at O site is relatively more favourable than the doping at Mn site. Therefore we consider doping at O site only in our subsequent calculations.

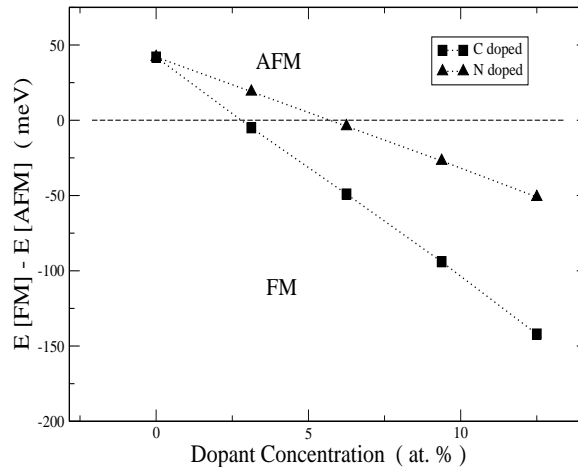


Figure 7.2: Energy difference between ferromagnetic and anti-ferromagnetic Mn-Mn couplings as a function of doping concentration.

Figure 7.2 shows the energy difference between ferromagnetic (FM) and anti-ferromagnetic (AFM) coupling between Mn atoms as a function of concentration of C and N. This energy difference is the measure of magnetic exchange interaction. It is evident from the figure that pure MnO in type II AFM state is favourable over FM state by above 42 meV/Mn atom. With the substitution of only one C atom at O site (equivalent to 3.125 at. % doping) ferromagnetic state becomes favourable over AFM state by about 5 meV/Mn atom.

With further increase in C concentration the stability of FM state further increases. In the case of doping by a single N atom, AFM state is still energetically favorable, however by small energy now (19 meV/Mn atom). This shows the tendency toward stabilization of FM state. FM state indeed stabilizes on increasing N concentration. At the concentration of 12.5 at. % (equivalent to substitution of 4 O atoms in the unit cell) FM state becomes favourable by 142 and 51 meV/Mn for C and N respectively. Thus, FM state is well stabilized in all the cases at doping concentration of 12.5 at.%.

Table 7.1: Magnetic moments (in μ_B) on Mn, X (X= C and N) and O for FM and AFM configurations at 12.5 at. % doping.

Dopant	FM			AFM		
	Mn	X	O	Mn	X	O
C	4.61, 4.72	-0.50	0.062, 0.078	4.61, 4.68	0.0	0.0
N	4.66, 4.72	-0.20	0.043, 0.100	4.63, 4.68	0.0	0.0

The atom projected magnetic moments for C and N dopings in FM and AFM configurations are listed in Table II. We find that the magnetic moment of 6 Mn atoms which are coordinated to the dopant decreases in both FM and AFM configurations. In AFM state the magnetic moment of the 6 coordinated Mn atoms decreases to 4.59 and 4.65 μ_B for C and N doping respectively. The corresponding values for FM state are 4.62 and 4.67 μ_B . However, the magnetic moment of other Mn atoms which are not coordinated with the dopant remains same (4.69 μ_B) in AFM configuration, but enhances to 4.72 μ_B in FM configuration. For the ferro-magnetically coupled Mn atoms, we observe a rather large anti-parallel moment on X atoms (-0.50, -0.20 μ_B for C and N respectively). However, in the AFM configuration, frustrating behaviour is observed at X and O sites. Due to the anti-parallel Mn moments the induced moments on X and O atoms disappear resulting in a zero magnetic moment in the unit cell.

In order to investigate the reason for stabilization of ferromagnetic state we have

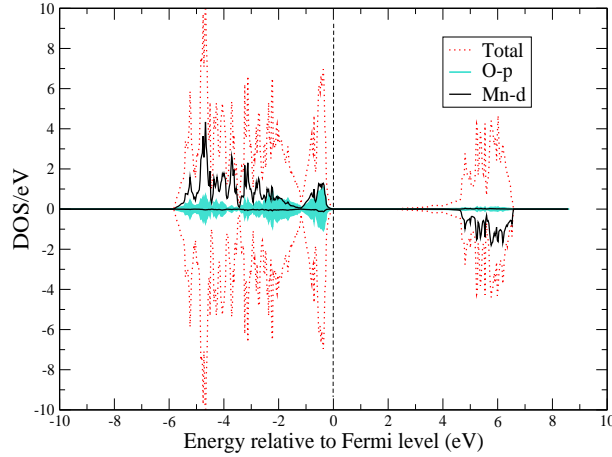


Figure 7.3: Density of states of pure MnO in type II AFM state. The dashed vertical line indicates the Fermi level (shifted to 0 eV). The total DOSs have been scaled down for the sake of clarity. Majority (up) spin states are plotted along positive y axis and minority (down) spin states along negative y axis.

analyzed the density of states (DOS) for both undoped and doped cases. Figure 7.3 shows the DOS in the AFM configuration for undoped MnO. The insulating character of MnO is well reproduced and the nature of DOS matches well with previous theoretical studies [106]. Here, the AFM super-exchange mediates the exchange coupling between the Mn atoms. The up spin $O-p$ states strongly hybridize with up spin d states of one Mn atom while the down spin $O-p$ states strongly hybridize with the down spin d states of neighboring Mn atoms and thereby lowering the energy more in the case of AFM state. This is the usual anti-ferromagnetic super-exchange mechanism [89, 90].

In Fig. 7.4, DOSs are shown for 12.5 at.% N and C doping in the FM state. The spin-polarized impurity states appear in the gap of MnO. Here one expects a competition between ferromagnetic double-exchange and anti-ferromagnetic super-exchange interactions between the Mn atoms. Both N and C- p states are exchange split thus providing some p states in the Fermi region which hybridize with Mn- d states. In the case of N doping [Fig. 7.4(left)], some of the up spin p states get unoccupied because an N atom sitting

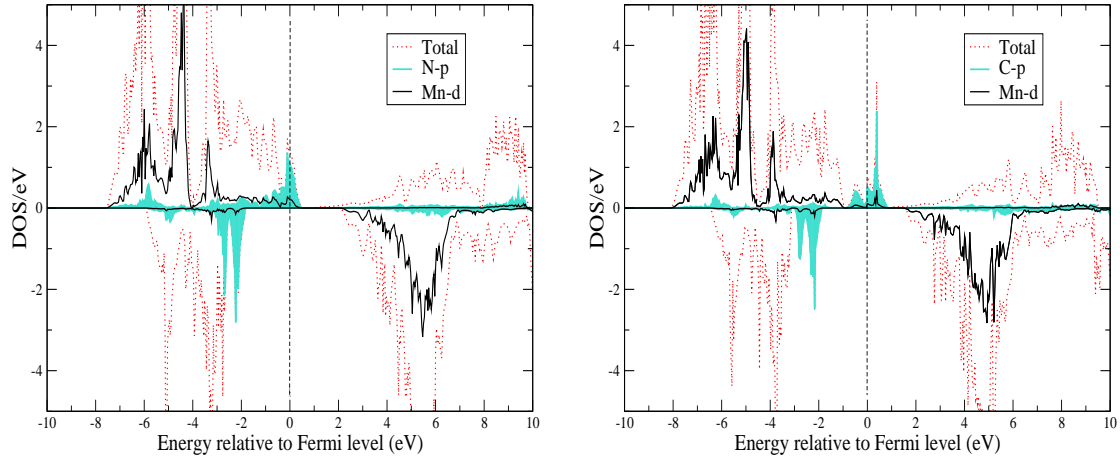


Figure 7.4: Density of states of 12.5 at. % doped MnO in FM state. (Left) N doped and (Right) C doped. The total DOSs have been scaled down for the sake of clarity. The dashed vertical lines indicate the Fermi levels (shifted to 0 eV). Majority (up) spin states are plotted along positive y axis and minority (down) spin states along negative y axis.

at O site provides one hole. In the case of C doping [Fig. 7.4(right)] some more up spin p states get unoccupied as a C atom sitting at O site provides 2 holes. When the concentration of N is low, the coupling between Mn atoms is still dominated by antiferromagnetic superexchange mechanism. As the concentration of N increases the concentration of hole increases and ferromagnetic coupling gets stabilized. For a particular doping concentration, C doping provides more holes than N doping and hence ferromagnetic state is more stabilized in the latter case. It should be noted that there is energy gap in down spin channel in both C and N doping cases. Thus, the FM state is of half metallic nature showing the possibility that C and N doped MnO can provide spin polarized current.

7.4 Summary

To summarize, we have shown that C and N doping at O sites of anti-ferromagnetic MnO can cause a ferromagnetic coupling between the Mn atoms. The carbon doping is

found to be more effective than N doping in stabilizing the ferromagnetism. The carbon concentration as low as 3.125 at. % could stabilize ferromagnetic state. Doping by C or N atom provides holes into the system which lead to stabilization of ferromagnetism. Ferromagnetic state in both C and N doped MnO is found to be of half metallic nature indicating its potential to produce spin polarized current. Since the stability of ferromagnetic state depends on the type of dopant atom and also on the doping concentration these parameters can be utilized as tools to control the transition temperature.

Chapter 8

Conclusion

We had set out to study the effect of doping in wide band gap semiconductors. The idea was to study structural, electronic and magnetic properties of these materials using the first principles method based on density functional theory. The motivation on one hand was to understand the experimental behavior from quantum chemical view point and on the other hand to explore new materials with desired properties. The systems for which experimental results are not available such microscopic understanding would be helpful in predicting the behaviour of the systems and would provide valuable information for the prospective experiment for the design of material with desired properties.

Our findings on pristine $(\text{ZnO})_n$ clusters reveal that the stability of clusters for $n \leq 7$ is mainly derived from linearity of O-Zn-O angle while for the larger clusters it is driven mainly from the increased coordination. For the first time we reported the tailoring of energy gap in ZnO clusters of sizes less than 1 nm. With the results on Mg/Cd doped ZnO clusters we explained the experimentally observed variation of band gap on the basis of nature of bonding and ionicity.

The study on Cr doped ZnTe clusters suggests the occurrence of ferromagnetic coupling between Cr atoms in the most stable structure. The increased hybridization between Cr-*d* and Te-*p* states lead to the stabilization of ferromagnetic state. When Cr atoms are farthest apart ferromagnetic and antiferromagnetic couplings are found to be degenerate

showing that the exchange coupling is short ranged.

In bulk ZnMnO and MnO we showed the stabilization of ferromagnetic state by doping with $2p$ elements. The doping with $2p$ elements at oxygen sites of these systems provides hole carriers into the system which lead to the stabilization of ferromagnetic state. These results are open for experimental verification.

There are, of course, still many loopholes which we should appreciate and attempt to eliminate in future work in this area. The very first problem arises with the density functional theory. Being based on a variational principle, it can only give the ground state properties. For example, the band gap requires the knowledge of the lowest excited state. Therefore, the DFT grossly underestimates the band gap. Accurate band gap estimations have been recently carried out by our group [107] but this has not been incorporated in this work. Incorporation of this within the VASP programme is a part of our continuing work. To look at the excited state spectrum we could carry out time dependent density functional approaches.

Even within the DFT framework, proper energy minimization and structure optimization requires extensive simulated annealing. This has not been adequately carried out to ascertain the geometries of the clusters. We have not tried to go beyond the DFT and carry out configuration interaction (CI) type chemical approaches for accurate energy determinations. CI for the larger clusters may not be very easy to carry out, but an attempt should be made.

Bibliography

- [1] M. Born and R. Oppenheimer, *Ann. Phys. (Leipzig)* **84**, 457 (1927).
- [2] L. H. Thomas, *Proc. Camb. Phil. Soc.* **23**, 542 (1927).
- [3] E. Fermi, *Z. Phys.* **48**, 37 (1928).
- [4] P. Hohenberg and W. Kohn, *Phys. Rev.* **136**, B864 (1964).
- [5] W. Kohn and L. J. Sham, *Phys. Rev.* **140**, A1133 (1965).
- [6] M. Gell-Mann and K. A. Brueckner, *Phys. Rev.* **106**, 364 (1957).
- [7] W. J. Carr, *Phys. Rev.* **122**, 1437 (1961).
- [8] P. Nozieres and D. Pines, *The Theory of Quantum Liquids*, (Benjamin, New York, 1966).
- [9] U. von Barth and L. Hedin, *J. Phys. Chem.* **5**, 1629 (1972).
- [10] S. H. Vosko, L. Wilk and M. Nusair, *Can. J. Phys.* **58**, 1200 (1980).
- [11] Y. Wang and J. P. Perdew, *Phys. Rev. B* **44**, 13298 (1991).
- [12] J. P. Perdew, K. Burke and M. Ernzerhof, *Phys. Rev. Lett.* **77**, 3865 (1996).
- [13] A. D. Becke, *Phys. Rev. A* **38**, 3098 (1988).
- [14] C. Lee, W. Yang and R. G. Parr, *Phys. Rev. B* **37**, 785 (1988).
- [15] W. C. Topp and J. J. Hopeld, *Phys. Rev. B* **7**, 1295 (1973).
- [16] D. R. Hamann, M. Schlüter and C. Chiang, *Phys. Rev. Lett.* **43**, 1494 (1979).

- [17] D. Vanderbilt, *Phys. Rev. B* **41**, 7892 (1990).
- [18] P.E. Blöchl, *Phys. Rev. B* **50**, 17953 (1994).
- [19] G. Kressé and D. Joubert, *Phys. Rev. B* **59**, 1758 (1999).
- [20] A. J. Hoffman, G. Mills, H. Yee and M. R. Hoffmann, *J. Phys. Chem.* **96**, 5546 (1992).
- [21] A. Kampmann and D. Lincot, *J. Electroanal Chem.* **418**, 73 (1996).
- [22] P.J. Sebastian and M. Ocampo, *Sol. Energy Mater. Sol. Cells* **44**, 1 (1996).
- [23] E. Corcoran, *Sci. Am.* **263**, 74 (1990).
- [24] J. M. Matxain, J. E. Fowler, and J. M. Ugalde, *Phys. Rev. A* **62**, 053201 (2000).
- [25] F. Calvo, *Phys. Rev. B* **67**, 161403(R) (2003).
- [26] J. M. Matxain, J. M. Mercero, J. E. Fowler, J. M. Ugalde, *Phys. Rev. A* **64**, 053201 (2001).
- [27] A.V. Bulgakov, I. Ozerov and W. Marine, (*preprint*) (2006).
- [28] E. C. Behrman, R. K. Foehrweiser, J. R. Myers, B. R. French and M. E. Zandler, *Phys. Rev. A* **49**, R1543 (1994).
- [29] F. Finocchi and C. Noguera, *Phys. Rev. B* **53**, 4989 (1995).
- [30] *CRC Handbook of Chemistry and Physics* (CRC, Boca Raton, 1977), 58th ed.
- [31] D. E. Manolopoulos, J. C. May and S. E. Down, *Chem. Phys. Lett.* **181**, 105 (1991).
- [32] M. Kabir and A. Mookerjee, *Phys. Rev. A* **69**, 043203 (2004).
- [33] E. M. Fernandez, J. M. Soler, I. L. Garzon, and L. C. Balbas, *Phys. Rev. B* **70**, 165403 (2004).
- [34] D. C. Reynolds, D. C. Look, and B. Jogai, *Solid State Communn.* **99**, 873 (1996).
- [35] D. C. Look, D. C. Reynolds, J. R. Sizelove, R. L. Jones, C. W. Litton, G. Cantwell, and W. C. Harsh, *Solid State Communn.* **105**, 399 (1998).

- [36] D. C. Reynolds, D. C. Look, B. Jogai, and H. Morkoc, *Solid State Communn.* **101**, 643 (1997).
- [37] S. krishnamoorthy, A. A. Iliadis, A. Inumpudi, S. Choopum, R. D. Vispute, T. Venkatesan, *Solid-State Electron.* **46**, 1633 (2002).
- [38] Z. Li, Y. Xiong and Y. Xie, *Inorg. Chem.* **42**, 24 (2003).
- [39] R.F. Mulligan, A. A. Iliadis and P. Kofinas, *Journal of Applied Polymer Science*, **89**, 1058 (2003).
- [40] M. H. Huang, S. Mao, H. Feick, H. Q. Yan, Y. Y. Wu, H. Kind, E. Weber, R. Russo and P. D. Yang, *Science* **292**, 1897 (2001).
- [41] H. Kind, H. Q. Yan, B. Messer, M. Law and P. D. Yang, *Adv. Mater.* **14**, 158 (2001).
- [42] W. Shan, J. W. Ager III, K. M. Yu, W. Walukiewicz, E. E. Haller, M. C. Martin, W. R. Mckinney and W. Yang, *J. Appl. Phys.* **85**, 8505 (1999).
- [43] C. N. R. Rao, G. U. Kulkarni, P. J. Thomas, P. P. Edwards, *Chem.-Euro. J.* **8**, 30 (2002).
- [44] A. Ohotomo, M. Kawasaki, T. Koida, K. Masubuchi, H. Koinuma, Y. Sakurai, T. Yasuda and Y. Segawa, *Appl. Phys. Lett.* **72**, 2466 (1998).
- [45] P. Sharma, A. Gupta, K. V. Rao, F. J. Owens, R. Sharma, R. Ahuja, J. M. Osorio Guillen, B. Johansson and G. A. Gehring, *Nature Mater.* **2**, 673677 (2003).
- [46] F. Wang, Z. Ye, D. Ma, L. Zhu and F. Zhuge, *J. Crystal Growth* **283**, 373 (2005).
- [47] T. Makimo, Y. Segawa, M. Kawasaki, A. Ohotomo, R. Shiroki, K. Tamura T. Yasuda and H. Koinuma, *Appl. Phys. Lett.* **78**, 1237 (2001).
- [48] L. M. Kukreja, S. Barik and P. Mishra *J. Crystal growth* **268**, 531 (2004).
- [49] Y. S. Wang, P. John Thomas, and P. O'Brien, *Phys. Chem. B Lett.* **110**, 21412 (2006).
- [50] R. Thangavel, M. Rajagopalan and J. Kumar, *Solid State Commun.* **137**, 507 (2006).

- [51] W. L. L. Lambrecht, S. Limpijumnong and B. Segall, *MRS Internet J. Nitride Semicond. Res.* **4s1**, G6.8 (1999).
- [52] R. Viswanatha, S. Sapra, B. Satpati, P. V. Satyam, B. N. Dev and D. D. Sarma, *J. Mater. Chem.* **14**, 661 (2004).
- [53] H. S. Kang, S. H. Lim, J. W. Kim, H. W. Chang, G. H. Kim, J. Kim, S. Y. Lee, Y. Li, J. Lee, J. K. Lee, M. A. Nastasi, S. A. Crooker and Q. X. Jia, *J. Crystal growth* **287**, 70 (2006).
- [54] J. C. Phillips, *Rev. Mod. Phys.* **42**, 317 (1970).
- [55] J. S. Nelson and I. P. Batra, *Phys. Rev. B* **39**, 3250 (1989).
- [56] C. R. A. Catlow and A. M. Stoneham, *J. Phys. C* **16**, 4321 (1983).
- [57] S. D. Bader, *Surf. Sci.* **500**, 172 (2002).
- [58] S. Sun, C. B. Murray, D. Weller, L. Folks, and A. Moser, *Science* **287**, 1989 (2000).
- [59] K. Raj and R. Moskowitz, *J. Magn. Magn. Mater.* **85**, 233 (1990).
- [60] J. A. Alonso, *Chem. Rev.* **100**, 637 (2000).
- [61] C. W. Zhang, Y. P. Feng and C. K. Ong, *Phys. Rev. B* **54**, 17208 (1996).
- [62] S. K. Nayak and P. Jena, *Phys. Rev. Lett.* **81**, 2970 (1998).
- [63] H. Liu, S. Wang, G. Zhou, J. Wu and W. Duan, *J. Chem. Phys.* **124**, 174705 (2006).
- [64] G. P. Das, B. K. Rao and P. Jena, *Phys. Rev. B* **69**, 214422 (2004).
- [65] H. Saito, V. Zayets, S. Yamagata and K. Ando, *Phys. Rev. Lett.* **90**, 207202 (2003).
- [66] T. M. Pekarek, J. E. Luning, I. Miotkowski and B. C. Crooker, *Phys. Rev. B* **50**, 16914 (1994).
- [67] K. Sato and H. Katayama-Yoshida, *Semicond. Sci. Technol.* **17**, 367 (2002).
- [68] D. Soundararajan, D. Mangalaraj, D. Nataraj, L. Dorosinskii and J. Santoyo-Salazar, *J. Phys. Conf. Series* **153**, 012048 (2009).

- [69] V. Kumar and Y. Kawazoe, *Phys. Rev. B* **65**, 073404 (2002).
- [70] C. Zener, *Phys. Rev.* **81**, 440 (1951).
- [71] Y. Liu and B. Liu, *J Phys. D Appl. Phys.* **40**, 6791 (2007).
- [72] X. H. Zhou, X. S. Chen, Y. Huang, H. Duan and W. Lu, *Phys. Status Solidi B* **243**, 1375 (2006).
- [73] H. Cheng and L. S. Wang, *Phys. Rev. Lett.* **77**, 51 (1996).
- [74] T. Dietl, H. Ohno, F. Matsukura, J. Gilbert and D. Ferrand, *Science* **287**, 1019 (2000).
- [75] Ü. Özgür, A. Teke, C. Liu, S.-J. Cho, H. Morkoc and H. O. Everitt *J. Appl. Phys.* **98**, 041301 (2005).
- [76] S. S. Kim, J. H. Moon, B. T. Lee, O. S. Song, J. H. Je, *J. Appl. Phys.* **95**, 454 (2004).
- [77] A. K. Pradhan, K. Zhang, S. Mohanty, J. B. Dadson, D. Hunter, J. Zhang, D. J. Sellmyer, U. N. Roy, Y. Cui, A. Burger, S. Mathews, B. Joseph, B. R. Sekhar, B. K. Roul, *Appl. Phys. Lett.* **86**, 152511 (2005).
- [78] K. Ueda, H. Tabata and T. Kawai, *Appl. Phys. Lett.* **79**, 988 (2001).
- [79] Z. Jin, T. Fukumura, M. Kawasaki, K. Ando, H. Saito, T. Sekiguchi, Y. Z. Yoo, M. Murakami, Y. Matsumoto, T. Hasegawa and H. Koinuma, *Appl. Phys. Lett.* **78**, 3824 (2001).
- [80] H.-J. Lee, S.-Y. Jeong, J.-Y. Hwang, and C. R. Cho, *Europhys. Lett.* **64**, 797 (2003).
- [81] R. Janisch, P. Gopal and N. A. Spaldin, *J. Phys.: Condens. Matter* **17**, R657 (2005).
- [82] N. A. Spaldin, *Phys. Rev. B* **69**, 125201 (2004).
- [83] X. C. Liu, E. W. Shi, Z. Z. Chen, H. W. Zhazng, B. Xiao and L. X. Song, *Appl. Phys. Lett.* **88**, 252503 (2006).

- [84] T. Zhang, L.-X. Song, Z.-Z. Chen, E.-W. Shi, L.-X. Chao and H.-W. Zhang, *Appl. Phys. Lett.* **89**, 172502 (2006).
- [85] K. Sato and H. Katayama-Yoshida, *Physica E* **10**, 251 (2001).
- [86] J. P. Perdew, J. A. Chevary, S.H. Vosko, K.A. Jackson, M. R. Pederson, D. J. Singh and C. Fiolhais, *Phys. Rev. B* **46**, 6671 (1992).
- [87] D. Iușan, B. Sanyal and O. Eriksson, *Phys. Status Solidi B* **229**, 673 (2006).
- [88] A. L. Rosa and R. Ahuja, *J. Phys.: Condens. Matter* **19**, 386232 (2007).
- [89] J. B. Goodenough, *J. Phys. Chem. Solids* **6**, 287 (1958).
- [90] J. Kanamori, *J. Phys. Chem. Solids* **10**, 87 (1959).
- [91] C. Zener, *Phys. Rev.* **82**, 403 (1951).
- [92] K. Sato, P. H. Dederichs, and H. Katayama-Yoshida, *J. Phys. Soc. Jpn.* **76**, 024717 (2007).
- [93] Gang H. Lee, Seung H. Huh, Jin W. Jeong, Byeong J. Choi, Seung H. Kim and Hyeon-C. Ri, *J Am. Chem. Soc.* **124**, 12094 (2002).
- [94] I.V. Solovyev and K. Terakura , *Phys. Rev. B* **58**, 15496 (1998).
- [95] S.K. Nayak and P. Jena, *J. Am. Chem. Soc.* **121**, 644 (1999).
- [96] V. I. Anisimov, M. A. Korotin and E. Z. Kurmaev, *J. Phys.: Condens. Matter* **2**, 3973 (1990).
- [97] B. Sanyal, O. Bengone and S. Mirbt, *Phys. Rev. B* **68**, 205210 (2003).
- [98] D. Iușan and B. Sanyal and O. Eriksson, *Phys. Rev. B* **74**, 235208 (2006).
- [99] V. V. Bannikov, I. R. Shein and A. L. Ivanovskii, *Technical Phys. Lett.* **33**, 541 (2007).
- [100] R. Q. Wu, L. Liu, G. W. Peng and Y. P. Feng, *Appl. Phys. Lett.* **86**, 122510 (2005).

- [101] M. A. Gorbunova, I. R. Shein, Y. N. Makurin, V.V. Ivanovskaya, V. S. Kijko and A. L. Ivanovskii, *Physica E* **41**, 164 (2008).
- [102] K. Kenmochi, V. A. Dinh, K. Sato, A. Yanase and H. Katayama-Yoshida, *J. Phys. Soc. of Japan* **73**, 2952 (2004).
- [103] S. L. Dudarev, G. A. Bottom, S. Y. Savrasov, C. J. Humphreys and A. P. Sutton, *Phys. Rev. B* **37**, 1505 (1998).
- [104] C. Franchini, V. Bayer, R. Podloucky, J. Paier and G. Kresse, *Phys. Rev. B* **72**, 045132 (2005).
- [105] G. Kressé and J. Furthmuller, *Compt. Mater. Sci.* **6**, 15 (1996).
- [106] O. Bengone, M. Alouani, P. Blöchl, and J. Hugel, *Phys. Rev. B* **62**, 16392 (2000).
- [107] M. Rahaman, S. Ganguli, P. Samal, M. K. Harbola, T. Saha-Dasgupta and A. Mookerjee, *Physica B* **404**, 1137 (2009).